THE ASTROPHYSICAL JOURNAL, 448:315–338, 1995 July 20

THE PRESUPERNOVA EVOLUTION AND EXPLOSION OF HELIUM STARS THAT EXPERIENCE MASS LOSS

S. E. WOOSLEY
Board of Studies in Astronomy and Astrophysics, UCO/Lick Observatory, University of California, Santa Cruz, CA 95064; and
General Studies Division, Physics Department, Lawrence Livermore National Laboratory

NORBERT LANGER
Max-Planck-Institut für Astrophysik, Karl-Schwarzschild-Strasse 1, D-85740 Garching bei München, Germany

AND

THOMAS A. WEAVER
General Physics Division, Physics Department, Lawrence Livermore National Laboratory, Livermore, CA 94550
Received 1994 June 6; accepted 1995 January 31

ABSTRACT

The evolution of helium stars with initial masses in the range 4–20 $M_\odot$ is followed through all stages of hydrostatic nuclear burning. We identify these objects as Wolf-Rayet stars that have lost their hydrogen envelopes, either before or early in their helium-burning phase, probably because they were in a mass-exchanging binary system or, for the more massive stars, because they were subject to a strong stellar wind. Stripped of their envelopes, these stars are subject to efficient (mass-dependent) mass loss. As a result, the final masses converge to a narrow range of small values: 2.26–3.55 $M_\odot$ for all stars considered. We identify these as progenitors of Type Ib and, perhaps, Type Ic supernovae and investigate the dependence of the presupernova structure on the initial mass of the helium star. For two models, the extra mass loss that could occur in a close binary, the product of common envelope evolution, is also considered. Five of our presupernova models are then exploded, using pistons, and their nucleosynthesis and bolometric light curves calculated. Peak luminosities are in the range (1.5–4) $\times 10^{42}$ ergs s^{-1}. The (unmodified) mass of ^{56}Ni for 10 explosions (variable parameterizations of explosion in the five stars) lies in a narrow range, 0.07–0.15 $M_\odot$. Other abundances from carbon through nickel are coproduced in approximately solar proportions along with interesting amounts of the long-lived radioactivities, ^{26}Al and ^{60}Fe. The light curves agree reasonably well with observations of Type Ib and Ic supernovae, including Type Ib SN 1983N and the recent Type Ic SN 1994I. A ^{56}Ni mass of $0.05^{+0.02}_{-0.01}$ $M_\odot$ is derived for the latter (for a distance of 7 Mpc), and speculations are presented regarding SN 1991bg. Ultimately, spectroscopic diagnostics of these models should aid in testing them.

Subject headings: nuclear reactions, nucleosynthesis, abundances — stars: evolution — stars: interiors — stars: mass loss — supernovae: general

1. INTRODUCTION

In a previous paper (Woosley, Langer, & Weaver 1993, hereafter WLW), we explored the presupernova evolution and explosion of single stars of high mass ($M_{ZAMS} \gtrsim 35\ M_\odot$), and, adopting efficient mass-dependent mass loss for the Wolf-Rayet stage (Langer 1989a, b), found that a significant fraction ended their lives as helium stars of small final mass ($\sim 4\ M_\odot$), i.e., as low-mass WC/WO stars. These were identified as possible progenitors of supernovae of Types Ib and Ic. It was also noted that the evolution of massive stars in close binaries might produce the same sort of supernova progenitor, a possibility that has been suggested many times (e.g., Wheeler & Levreault 1985; Uomoto 1986; Podsiadlowski, Joss, & Hsu 1992). In this paper, we model the evolution and fate of massive helium stars which might have been born in close binary systems and examine the similarities and differences of their final stages and potential supernova explosions with the corresponding stages of single-star descendants.

When a massive star finishes core hydrogen burning, its radius increases on roughly a thermal timescale ($\sim 10^4$ yr) as it evolves to become a supergiant (e.g., Schaller et al. 1992). Therefore, in a close binary system, when the stellar volume is limited by the Roche volume, the primary (initially more massive) component will, upon leaving the main sequence, experience drastic mass loss due to Roche lobe overflow. This may lead to complete loss of the hydrogen-rich envelope during a time which is short compared to the timescale for core helium burning (Vanbeveren 1991; Podsiadlowski et al. 1992; de Loore & De Greve 1992; De Greve & de Loore 1992; Woosley et al. 1994). The resulting objects can be well approximated by chemically homogeneous pure helium stars (with trace elements according to the initial metal content and mass of the primary). This simplification allows the study of their evolution independent of the previous phases of core hydrogen burning and Roche lobe overflow (e.g., Vanbeveren 1991).

Whether a given massive close binary system will produce a helium star obviously depends on the stellar mass ratio and the orbital parameters (de Loore & De Greve 1992). It also depends sensitively on the stellar metallicity and on the treatment of convection. Both are known to drastically affect the radius evolution beyond core hydrogen exhaustion (cf. Schaller et al. 1992, for Z dependence; Langer 1991, for the dependence on the convection model), and this makes it hard to estimate the fraction of all binaries that is able to generate helium stars. However, there are numerous observations suggesting that a considerable number of helium stars are being produced in the Galaxy and the Magellanic Clouds (Vrancken et al. 1991; Maeder 1991; Smith & Maeder 1991; De Greve & de Loore

1992; Vanbeveren & de Loore 1993). This is particularly true for the relatively high number of Wolf-Rayet (W-R) stars in the SMC.

In this paper we shall not discuss the formation phase or the formation rate of helium stars (see Podsiadlowski et al. 1992; Tutukov, Yungelson, & Iben 1992; Hsu et al. 1995), but will simply assume that they exist and investigate their further evolution. In any case, assuming the complete loss of the hydrogen envelope near or prior to helium ignition is an interesting limit. Should it turn out that the last vestige of the hydrogen envelope is actually lost much later, i.e., toward the end of helium core burning, the resulting structure will be intermediate between the helium stars studied here and the single stars modeled in WLW (see also Nomoto & Hashimoto 1988; Hashimoto et al. 1993; Thielemann, Nomoto, & Hashimoto 1993).

As with single stars, once the hydrogen envelope is entirely lost, the remaining helium star may be identified as a W-R star. Further mass loss then affects the helium-burning phase of evolution considerably (§ 2), but should be negligible after carbon ignition. This allows the evolution to be examined in two stages, a mass-losing phase in which the nuclear physics is relatively simple and a more complex later evolution computed at constant mass (§ 3). The simulated explosions of the resulting presupernova models are discussed in § 4.

2. PRE–CARBON-BURNING EVOLUTION AND MASS LOSS

2.1. *Physics of the Calculation*

As in WLW, the evolution of the stars prior to carbon ignition is followed using the Göttingen stellar evolution code. Its main features are unaltered with respect to WLW, and we need only review them briefly.

The mass-loss rate employed during helium burning (up to carbon ignition) is that of Langer (1989b). Specifically, $\dot{M} = -kM^{2.5}$ (with M in $M_\odot$ and $\dot{M}$ in $M_\odot$ yr^{-1}) and $k = 6 \times 10^{-8}$, so long as the carbon surface mass fraction does not exceed 0.02, and $k = 10^{-7}$ afterward.

The identification of our more massive models with W-R stars (and consequently the use of Wolf-Rayet mass-loss rates) are well justified (Langer 1989b; Lamers et al. 1991). While the loss rate employed for the smaller masses considered here is less certain, the masses derived for W-R stars on the basis of their mass-luminosity relation (Maeder 1983; Langer 1989a; Schaerer & Maeder 1992) can be as small as $\sim 4\ M_\odot$ (van der Hucht 1992; Hamann, Koesterke, & Wessolowski 1993) without showing any major deviation from the general mass-loss relation. A recent linear analysis of pulsational instability (Glatzel, Kiriakidis, & Fricke 1993) showed helium stars above $\sim 4\ M_\odot$ to be unstable with respect to radial pulsations with a growth time of order only few dynamical timescales. Such instabilities are a possible physical explanation of the strong W-R wind observed for He stars with $M \gtrsim 4\ M_\odot$ and might imply a pile-up of final masses near this value (Langer et al. 1994).

Convective and semiconvective mixing are also modeled as in WLW: we use the Ledoux criterion for convection and perform "slow" semiconvective mixing in convectively stable superadiabatic layers. However, in contrast to ordinary stars, which have constant or even growing helium cores as a consequence of hydrogen shell burning, the convective core mass here decreases during core helium burning due to the decreasing total mass. As a result, semiconvection has little effect on these stars, and the core helium burning phase of evolution is not sensitive to choices of convection criterion and semiconvective mixing speed (§ 2.4).

For the $^{12}C(\alpha, \gamma)^{16}O$ nuclear reaction rate we followed Weaver & Woosley (1993) in choosing a value 1.7 times that of Caughlan & Fowler (1988). This gives the tightest fit of massive star nucleosynthesis to solar system abundances and is consistent with current experimental determinations (Azuma et al. 1994).

Nuclear reactions followed during helium burning were the 3α-reaction, and (α, γ) on ^{12}C, ^{16}O, ^{20}Ne, ^{24}Ng, ^{14}N, and ^{18}O. The nucleosynthesis of isotopes of Ne, Mg, and Si was also followed approximately, and the neutron flux estimated by incorporating the neutron sources $^{22}Ne(\alpha, n)^{25}Mg$, $^{21}Ne(\alpha, n)^{24}Mg$, $^{25}Mg(\alpha, n)^{28}Si$, and $^{26}Mg(\alpha, n)^{29}Si$ and the neutron sinks ^{20}Ne, ^{21}Ne, ^{24}Mg, ^{25}Mg, ^{28}Si, and ^{29}Si. This allows a good estimate of the neutron exposure, $\tau_n = \int n_n v_T\, dt$, during helium burning. The exposure τ_n and the abundances of several key isotopes at the end of helium burning are plotted in Figure 4 later in the paper.

2.2. *Evolution Prior to Carbon Ignition*

The time evolution of mass-losing helium stars with initial masses of 20, 15, 10, 7, 6, 5, and 4 $M_\odot$ was first computed up to carbon ignition. For the initial abundances, a mass fraction of metals of 0.02 was adopted with a relative distribution of heavy elements as given by Anders & Grevesse (1989). However, for the CNO isotopes we used the CNO equilibrium distribution (cf. Clayton 1968) that would result from previous hydrogen burning. Table 1 lists the isotopes considered during core helium burning and the adopted composition.

The thermal and mechanical structure of a helium or W-R star during core helium burning is almost completely determined by its current mass (Langer 1989a). Therefore, the time evolution of the stellar mass (Fig. 1) determines the evolution of our sequences in the H-R diagram as well as in the T_c-ρ_c diagram (Figs. 2 and 3).

Figure 1 shows the mass convergence that happens for all our models. The final mass in each case is almost independent

TABLE 1

INITIAL ABUNDANCES FOR CORE HELIUM BURNING

Isotope	Initial Abundance
^{1}H.....	0
^{4}He	0.984
^{12}C.....	2.95E−4
^{13}C.....	8.96E−5
^{14}N	1.17E−2
^{15}N	3.37E−7
^{16}O	2.64E−4
^{17}O	2.00E−5
^{18}O	8.40E−9
^{20}Ne	1.62E−3
^{21}Ne	4.13E−6
^{22}Ne	1.32E−4
^{23}Na	3.34E−5
^{24}Mg.....	5.17E−4
^{25}Mg.....	6.79E−5
^{26}Mg.....	7.78E−5
^{27}Al	5.80E−5
^{28}Si	6.54E−4
^{29}Si	3.42E−5
^{30}Si	2.36E−5

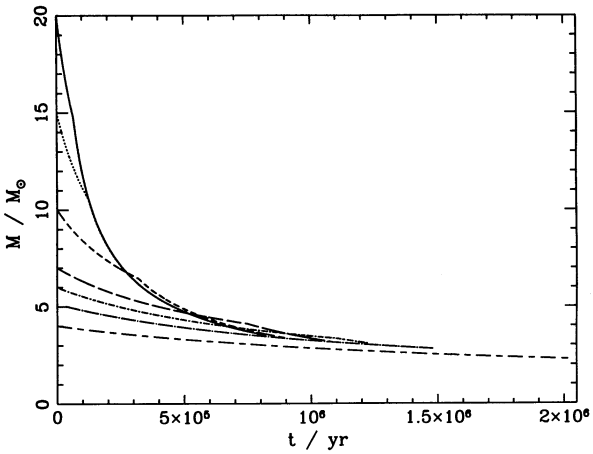

FIG. 1.—Total stellar mass as function of time for our sequences with initial masses of 20, 15, 10, 7, 6, 5, and 4 $M_\odot$. Mass convergence due to mass-dependent mass loss is clearly visible.

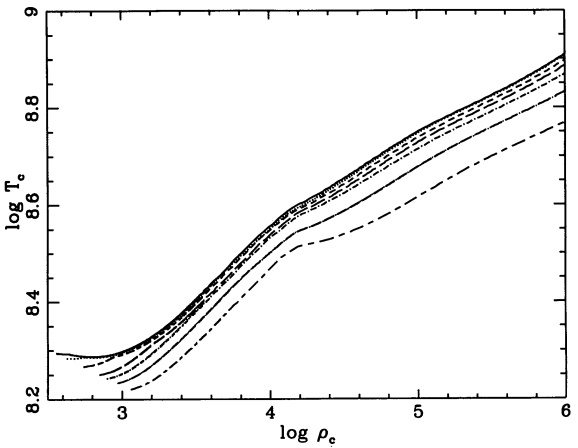

FIG. 3.—Evolution of the sequences shown in Fig. 1 in the (log T_c, log ρ_c)-diagram. Note the tight convergence of the more massive tracks in contrast to the quite different evolution of the stars with lowest initial masses.

of its initial value (see also Table 2). Final masses are in the range 3.55–2.26 $M_\odot$. The convergence is best for the stars with highest initial masses—e.g., the 15 and 20 $M_\odot$ sequences are almost indistinguishable at the end; cf. Table 2—while the 4 and 5 $M_\odot$ sequences show significant differences during core helium burning, and even more later on. The reason is that the conditions for mass convergence; i.e., especially the composition independence of the internal structure, are less well fulfilled for helium stars of lower mass (Langer 1989a). This trend is also apparent in Figures 2 and 3, where the initially more massive stars converge following core helium exhaustion at log $L/L_\odot = 4.5$ and log $T_s = 5$, and at log $T_c = 8.55$ and log $\rho_c = 4.2$, respectively, while the 4 and 5 $M_\odot$ sequences deviate considerably.

In WLW it was shown that, while the thermal and mechanical structures of helium-burning helium stars do not keep a memory of their initial mass, the chemical composition does. This can result in divergent post–helium-burning evolution even for stars of identical final mass (cf. Fig. 6 of WLW). This same behavior is found again in the present calculations and is again more prominent for lower initial masses. As a consequence, the stellar radii at the time of carbon ignition, for example, do depend on the initial mass (Table 2 and Fig. 2), ranging from $R_G \simeq 1\ R_\odot$ for the highest initial masses considered to $R_G \simeq 9\ R_\odot$ for $M_i = 4\ M_\odot$. Also, the central conditions depend somewhat on the initial mass (see Fig. 3). For example, in Table 2 we show the mass of the carbon-oxygen core at a central temperature of 5×10^8 K. For $M_i = 4\ M_\odot$, this mass is only 1.29 $M_\odot$, i.e., less than the Chandrasekhar mass, while it ranges from 1.57 to 2.11 $M_\odot$ for larger initial masses. This makes the late evolution of our 4 $M_\odot$ sequence quite different from the more massive stars (§ 3).

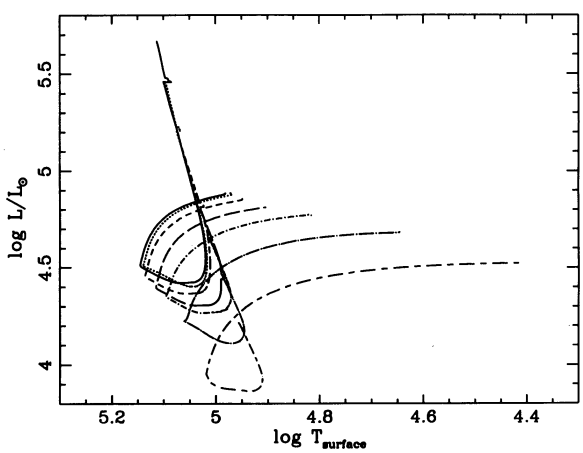

FIG. 2.—Evolution of luminosity vs. stellar surface temperature for the sequences shown in Fig. 1. Line styles are chosen as in Fig. 1 for the corresponding sequences; i.e., the solid line corresponds to the 20 $M_\odot$ track, and the long-dash–short-dashed line corresponds to the 4 $M_\odot$ sequence.

2.3. *Chemical Structure at Carbon Ignition and Stellar Wind Ejecta*

The composition of our models prior to carbon ignition (Figs. 4 and 5) is determined by (1) the convective core size, (2) mass loss, and (3) beyond core helium exhaustion, by helium shell burning. The mass of the convective core of helium stars is smaller in both absolute mass and relative size for smaller stellar mass. For example, the initial mass of the convective core is $\sim 2\ M_\odot$ for our 4 $M_\odot$ sequence, but is 15 $M_\odot$ for the 20 $M_\odot$ helium star (see also Langer 1989a). During rapid mass loss, the convective core recedes with time (see § 2.4 for the 4 and 5 $M_\odot$ sequences), producing a smooth helium gradient of order $\Delta Y/\Delta M_r \simeq 1/(M_i - M_f)$. Since the mass-loss rates are much larger for higher initial masses, the helium gradient is shallower for high mass. It is $1/(M_i - M_f) = 0.06$ for the 20 $M_\odot$ sequence, but 0.6 for the 4 $M_\odot$ sequence. Because the 3α-reaction dominates over $^{12}C(\alpha, \gamma)^{16}O$ during early helium burning we find, in the outer part of the inhomogeneous envelopes of our stars, a carbon gradient of opposite sign: $\Delta C/\Delta M_r \simeq -\Delta Y/\Delta M_r$. Note that the slope of the helium profile is important for the speed at which the carbon-oxygen core grows due to shell helium burning and therefore for the final size of the carbon-oxygen core (see also WLW).

Owing to the large mass-loss rates of our massive helium stars (the initial loss rate for our 20 $M_\odot$ model is $10^{-4}\ M_\odot\ yr^{-1}$) and the large size of the convective core in these cases, products of core helium burning appear at the stellar surface relatively early during core helium burning. Furthermore, the final helium surface mass fraction is relatively low (~ 0.35; Table 2), and carbon is very abundant ($C_s \simeq 0.50$). The low-

TABLE 2

KEY QUANTITIES FOR THE COMPUTED SEQUENCES

M_i ($M_\odot$) (1)	M_f ($M_\odot$) (2)	τ_{He} (10^5 yr) (3)	τ_{rest} (10^4 yr) (4)	Y_s (5)	C_s (6)	O_s (7)	C_c (8)	$M^s_{C/O}$ ($M_\odot$) (9)	$M^f_{C/O}$ ($M_\odot$) (10)	M_{Fe} ($M_\odot$) (11)	R_G ($R_\odot$) (12)	R_{link} ($R_\odot$) (13)
20	3.55	7.74	4.0	0.34	0.51	0.12	0.33	2.11	2.55	1.48	1.0	0.31
15	3.51	7.82	3.7	0.36	0.51	0.11	0.34	2.09	...	...	1.1	0.67
10	3.35	8.65	4.3	0.36	0.51	0.11	0.34	2.00	2.52	1.48	1.1	0.92
7.....	3.20	10.3	4.0	0.68	0.28	0.02	0.35	1.91	2.29	1.41	1.3	0.55
6.....	3.10	11.7	5.0	0.89	0.09	2.7–3	0.37	1.80	...	...	1.9	0.93
5.....	2.82	14.1	8.0	0.98	1.0–3	2.8–4	0.38	1.57	1.86	1.37	3.8	0.91
4.....	2.26	18.9	14	0.98	3.6–4	2.6–4	0.40	1.29	1.53	1.34	9.1	9.1
5X.....	2.75	14.9	6.0	0.98	5.0–3	3.4–4	0.38	1.58	...	...	3.7	0.99
4X.....	2.21	20.4	13	0.98	5.6–4	2.7–4	0.39	1.28	...	...	8.9	8.9

NOTE.—Cols. (1) Initial mass of He star; (2) final mass; (3) He-burning lifetime; (4) approximate post–He-burning lifetime; (5) final surface He abundance; (6) final surface carbon abundance; (7) final surface oxygen abundance; (8) central carbon mass fraction at core He exhaustion; (9) C/O core mass at $T_c = 5 \times 10^8$ K; (10) final C/O core mass; (11) iron core mass; (12) final radius of Göttingen sequences ($T_c \simeq 10^9$ K); (13) radius at time of link ($T_c \simeq 5 \times 10^8$ K).

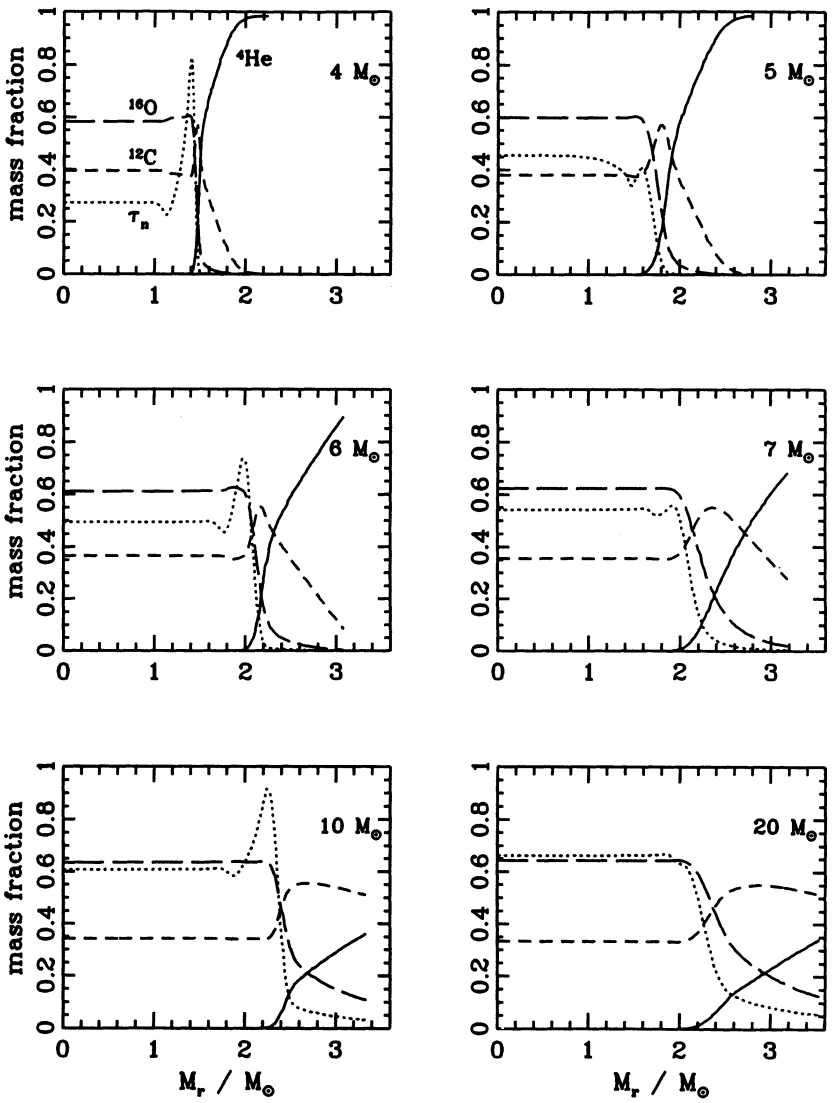

FIG. 4.—Internal mass fractions of He (*solid line*), C (*short-dashed line*), and O (*long-dashed line*) as a function of the Lagrangian mass coordinate for the last models of our sequences which were computed with the Göttingen code, i.e., prior to central carbon ignition, for initial masses of 4, 5, 6, 7, 10, and 20 $M_\odot$. The dotted line is the neutron exposure τ_n in units of 2×10^{26} cm^{-2}.

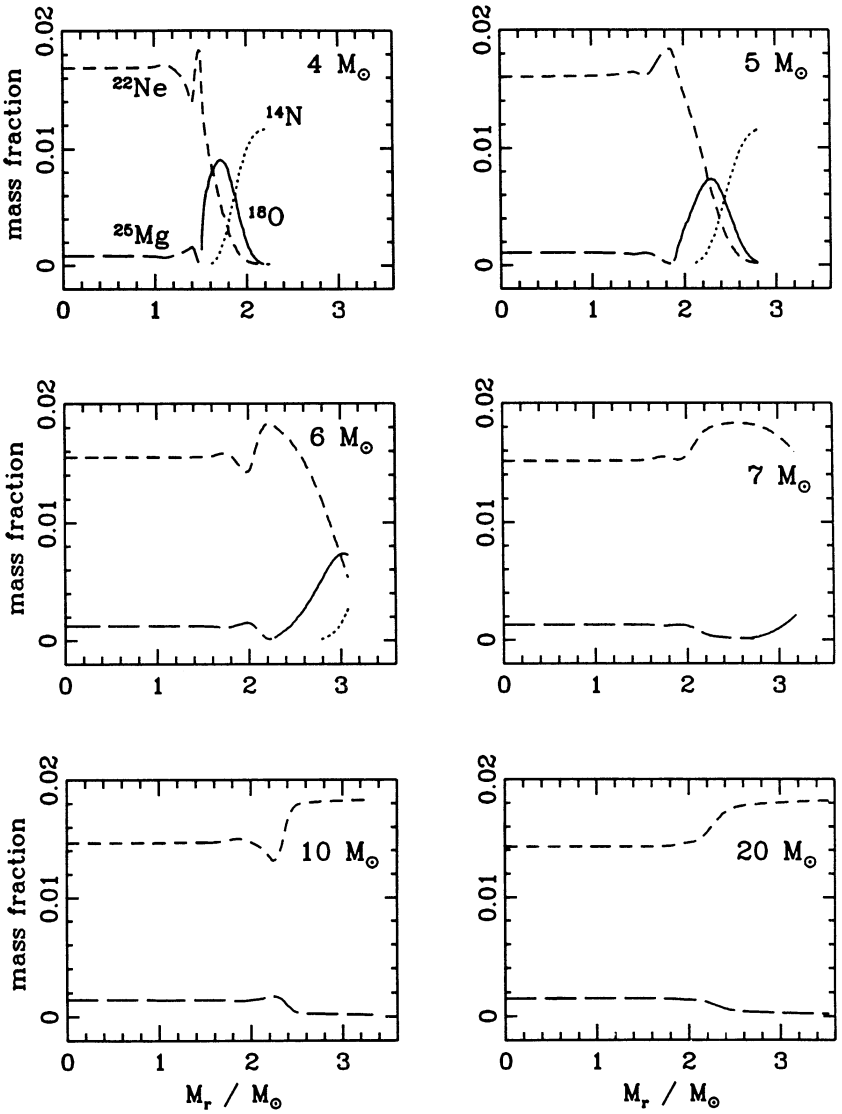

FIG. 5.—Internal mass fractions of ^{14}N (*dotted line*), ^{18}O (*full line*), ^{22}Ne (*short-dashed line*), and ^{25}Mg (*long-dashed line*) as a function of the Lagrangian mass coordinate for the last models of our sequence, which were computed with the Göttingen code, i.e., prior to central carbon ignition, for initial masses of 4, 5, 6, 7, 10, and 20 $M_\odot$.

mass sequences, on the other side, do not achieve the evolutionary status of a WC star. Their surface abundances remain nearly unaltered throughout the evolution.

As a consequence, the enrichment of the interstellar medium resulting from the stellar wind of our models is different for high- and low-mass stars. This can be seen in Table 3A which gives the total mass of ejected matter $M_{\rm wind}(X_i)$ for each isotope X_i calculated assuming $M_{\rm wind}(X_i) = \int X_{i,s}(t)\dot{M}\,dt$, with $X_{i,s}$, the surface mass fraction of the ith isotope. These numbers are also converted into production factors, $f_i = M_{\rm wind}(X_i)/[(M_i - M_f)X_{i,\odot}]$. Table 3B clearly shows that for small masses it is just the assumed CNO processing during hydrogen burning (§ 2.2) that leads to production factors different from unity. On the other hand, more massive sequences efficiently eject several isotopes newly synthesized during helium burning, including ^{12}C, ^{18}O, and ^{22}Ne. Some of the more massive models even have winds that are enriched in ^{25}Mg, ^{26}Mg, ^{29}Si, and ^{30}Si and the *s*-process (Figs. 4 and 5).

Note that we do not consider any of the nucleosynthesis that occurs in the hydrogen envelopes of the progenitor stars of our helium cores. Much of this envelope may be transferred to the companion star during Roche lobe overflow, in contrast to the mass lost during core helium burning, which is readily expelled into the interstellar medium.

2.4. *Models Computed Using the Schwarzschild Criterion*

As mentioned in § 2.1, we used the Ledoux criterion for convection (plus slow semiconvective mixing in superadiabatic regions) in our standard calculations. In order to test the sensitivity of our results to this assumption during helium burning (see also § 3.1), we computed two additional models for initial helium masses of 4 and 5 $M_\odot$ using the Schwarzschild criterion for convection (sequences 4X and 5X in Tables 2 and 3).

As Tables 2 and 3 show, models of the same initial mass computed with the different assumptions regarding convection are very similar. There is a slight increase in the convective core

TABLE 3A

PRODUCTION FACTORS IN THE WIND MATTER

	M_i								
ISOTOPE	20	15	10	7	6	5	4	5X	4X
^{4}He	2.91	2.89	3.01	3.39	3.50	3.52	3.52	3.52	3.52
^{12}C.....	43.3	44.5	35.3	9.59	1.41	0.09	0.08	0.12	0.09
^{14}N	3.85	5.02	7.36	10.6	12.8	13.6	13.6	13.5	13.5
^{16}O	1.88	2.08	1.81	0.22	0.05	0.03	0.03	0.03	0.03
^{18}O	61.0	54.7	58.0	86.1	38.3	0.36	0.05	1.92	0.82
^{20}Ne	1.00	1.00	1.00	1.00	1.00	1.00	1.00	1.00	1.00
^{21}Ne	1.24	1.19	1.10	1.01	1.00	1.00	1.00	1.00	1.00
^{22}Ne	92.1	80.9	56.1	18.5	3.29	1.01	1.00	1.05	1.00
^{24}Mg.....	0.98	0.98	0.99	1.00	1.00	1.00	1.00	1.00	1.00
^{25}Mg.....	1.49	1.40	1.20	1.01	1.00	1.00	1.00	1.00	1.00
^{26}Mg.....	1.65	1.57	1.33	1.03	1.00	1.00	1.00	1.00	1.00
^{28}Si	0.99	0.99	0.99	1.00	1.00	1.00	1.00	1.00	1.00
^{29}Si	1.23	1.19	1.10	1.01	1.00	1.00	1.00	1.00	1.00
^{30}Si	1.08	1.06	1.03	1.00	1.00	1.00	1.00	1.00	1.00

TABLE 3B

AMOUNT OF MATTER LOST IN THE STELLAR WIND (in $M_\odot$)

	M_i								
ISOTOPE	20	15	10	7	6	5	4	5X	4X
^{4}He	13.4	9.28	5.61	3.60	2.84	2.15	1.71	2.21	1.76
^{12}C.....	2.50	1.79	8.25(−1)	1.28(−1)	1.43(−2)	6.83(−4)	5.16(−4)	9.69(−4)	5.38(−4)
^{14}N	5.46(−2)	4.97(−2)	4.23(−2)	3.46(−2)	3.19(−2)	2.56(−2)	2.04(−2)	2.62(−2)	2.09(−2)
^{16}O	2.42(−1)	1.87(−1)	9.34(−2)	6.61(−3)	1.08(−3)	5.77(−4)	4.58(−4)	5.96(−4)	4.70(−4)
^{18}O	1.71(−2)	1.07(−2)	6.56(−3)	5.56(−3)	1.89(−3)	1.34(−5)	1.37(−6)	7.33(−5)	2.49(−5)
^{20}Ne	2.66(−2)	1.86(−2)	1.08(−2)	6.15(−3)	4.70(−3)	3.55(−3)	2.82(−3)	3.64(−3)	2.90(−3)
^{21}Ne	8.50(−5)	5.65(−5)	3.01(−5)	1.58(−5)	1.20(−5)	9.05(−6)	7.19(−6)	9.28(−6)	7.38(−6)
^{22}Ne	1.97(−1)	1.21(−1)	4.85(−2)	9.21(−3)	1.24(−3)	2.87(−4)	2.26(−4)	3.07(−4)	2.33(−4)
^{24}Mg.....	8.33(−3)	5.84(−3)	3.41(−3)	1.96(−3)	1.50(−3)	1.13(−3)	9.00(−4)	1.16(−3)	9.24(−4)
^{25}Mg.....	1.66(−3)	1.09(−3)	5.42(−4)	2.61(−4)	1.97(−4)	1.49(−4)	1.18(−4)	1.53(−4)	1.21(−4)
^{26}Mg.....	2.11(−3)	1.40(−3)	6.89(−4)	3.03(−4)	2.26(−4)	1.70(−4)	1.35(−4)	1.75(−4)	1.39(−4)
^{28}Si	1.06(−2)	7.42(−3)	4.32(−3)	2.48(−3)	1.90(−3)	1.43(−3)	1.14(−3)	1.47(−3)	1.17(−3)
^{29}Si	6.94(−4)	4.68(−4)	2.50(−4)	1.31(−4)	9.92(−5)	7.49(−5)	5.95(−5)	7.69(−5)	6.11(−5)
^{30}Si	4.18(−4)	2.88(−4)	1.62(−4)	8.98(−5)	6.85(−5)	5.17(−5)	4.11(−5)	5.30(−5)	4.22(−5)
Total.....	16.446	11.485	6.652	3.799	2.900	2.183	1.740	2.248	1.787

size toward the end of core helium burning for the models that used the Schwarzschild criterion. This happens because of the very small mass-loss rates in this case ($\sim 4 \times 10^{-7}\ M_\odot\ \mathrm{yr}^{-1}$) and leads to a lengthening of the helium-burning time by $\sim 6\%$. The final masses differ by only 2%. It is also obvious from Tables 2, 3A, and 3B that the convection model is even less important for the 5 $M_\odot$ case than it is for the 4 $M_\odot$ case. For $M_i = 20$–6 $M_\odot$ it should be completely unimportant.

In summary, the choice of the convection criterion and the efficiency of semiconvective mixing has almost no effect on the evolution of our sequences prior to carbon ignition. Owing to the fact that the stellar mass has no time to change during subsequent burning stages, the situation could be different there (§ 3.1 and Fig. 10 below).

2.5. *Comparison with Single-Star Evolution*

The lower mass helium stars studied here are probably the result of close binary evolution, but very massive single stars may also lose their envelopes before exploding (cf. WLW). Here we briefly discuss two basic differences that can be expected in the final structure of the two kinds of models.

The first difference results because in the single-star case the initial mass range for which loss of the entire hydrogen envelope occurs is restricted to the largest initial masses, i.e., $M_{\mathrm{ZAMS}} \gtrsim 30\ M_\odot$ at $Z = 0.02$ (Schaller et al. 1992; WLW) and $M_{\mathrm{ZAMS}} \gtrsim 60\ M_\odot$ at $Z = 0.008$ (Schaerer et al. 1993). For close binary stars, in principle, primary components with $M_{\mathrm{ZAMS}} \gtrsim 10\ M_\odot$ could both lose their envelopes and evolve to iron core collapse. Further, this occurrence would be approximately independent of their initial metallicity. Thus, on the average the original supernova progenitor may have been considerably less massive in those systems where envelope loss occurs by mass exchange. Many such stars will still possess a substantial mantle of pure helium at the time of their explosion (e.g., our 4 and 5 $M_\odot$ sequences; Figs. 4*a* and 4*b*). On the other hand, most Type I supernovae resulting from *single* stars that have lost their envelopes will come from stars with $M_{\mathrm{ZAMS}} \gtrsim 30\ M_\odot$, i.e., from helium cores with $M \gtrsim 10\ M_\odot$, and in achieving the characteristic low final mass, their surface will be greatly enriched in carbon and possibly also in oxygen (Figs. 4*c*–4*f*; WLW, Figs. 1*c*–1*f*).

Second, for helium stars the rapid (mass-dependent) mass loss starts, by assumption, immediately at the beginning of core helium burning. In the single-star case, a substantial fraction of the helium-burning lifetime may be spent before the hydrogen-rich envelope is lost. It was shown in WLW that the

hydrogen envelope has to be completely lost before the central helium mass fraction is reduced to $Y_c \simeq 0.50$ in order to approach the regime of mass convergence. Even if the hydrogen envelope is lost before $Y_c = 0.50$, the final mass will remain somewhat larger than for helium stars. For example, in the 60 $M_\odot$ sequences of WLW the mass of the stars at the time of vanishing surface hydrogen abundance was $\sim 23\ M_\odot$. However, since this occurs only at $Y_c = 0.65$, the final masses were in the range 4.25–6.65 $M_\odot$ [depending on the $^{12}C(\alpha, \gamma)^{16}O$ nuclear reaction rate] which is similar to but significantly larger than 3.55 $M_\odot$, the final mass of our 20 $M_\odot$ helium star. Thus, Type I supernova progenitors in interacting binaries will, on average, have smaller masses than those coming from single stars. This is a consequence of both the early onset of rapid mass loss and the smaller initial helium core mass in the binary stars.

Another interesting effect of the early loss of the *complete* H-rich envelope is major overproduction of ^{18}O. If part of the hydrogen envelope remains on the star during early helium burning, much of the ^{18}O produced from ^{14}N by α-capture will be mixed into the growing convective core and destroyed. This is prevented when the hydrogen envelope is lost very early, since in that case the helium core mass decreases due to the W-R mass loss and so does the convective core mass. Consequently, large amounts of ^{18}O are ejected into the interstellar medium rather than being converted into ^{22}Ne (Table 3, and Table 11 below).

To summarize, Type I supernova progenitors resulting from massive stars in close binary systems will be, on the average, less massive and present a less evolved surface at the time of the explosion than those derived from single stars. This is seen in Table 4, where amount and composition of the supernova ejecta of our helium star models (which are exploded in § 4) are compared with those of a typical low-mass remnant resulting from massive single-star evolution and with a typical Type Ia model. Focusing on the low-mass helium star models, which are statistically most important due to initial-mass function effects, we see the ejecta of Type I supernovae derived from massive close binaries are expected to contain relatively small amounts of silicon, but considerable amounts of helium, and at least some oxygen. The characteristic spectral features of Type Ib supernovae suggest that this may be the case (e.g., Wheeler 1990).

3. POST–HELIUM-BURNING EVOLUTION

As in WLW the advanced stages of stellar evolution were followed using the KEPLER code (Weaver, Zimmerman, & Woosley 1978, and references in WLW). Models were transferred from the Göttingen code when the central temperature had risen to 5×10^8 K. Subsequent evolution was assumed to be sufficiently rapid that further mass loss could be ignored. Unlike in WLW, however, the evolution of the composition was followed in detail here—a nuclear reaction network of 200 isotopes (Table 5) being employed in each zone of the star following the link at helium depletion. This allows an accurate description of nucleosynthesis for all *primary* isotopes produced either in the advanced burning stages or the supernova explosion itself.

Secondary nuclei whose abundances are altered by hydrogen or helium burning are, of course, not well tracked by this procedure. As a check on the calculation and also to properly estimate the nucleosynthesis of *secondary* isotopes, one model (model 7K) was calculated using the KEPLER code and 200 isotope network for the entire evolution (including hydrogen and helium burning). These results are discussed in §§ 3.1 and 4.2.

Semiconvection during carbon burning and more advanced stages was treated, in the standard cases, as in WLW. Specifically the Ledoux criterion was employed for convective mixing with the semiconvective diffusion coefficient parameterized as in Woosley & Weaver (1988). The factor F in their equation (1) was taken equal to 10^{-4}. This gives a diffusion coefficient comparable to that used in the Göttingen code and corresponds to what Weaver & Woosley (1993) have called "restricted" semiconvection. In one case, model 10S, the semiconvective diffusion coefficient was taken to be 1000 times greater ($F = 0.1$ in Woosley & Weaver 1988; "nominal" in Weaver & Woosley

TABLE 4

SUPERNOVA EJECTA (in $M_\odot$)

M_i	M_f	M_{ejecta}	M_{He}	M_O	M_{Si}	$M_{^{56}Ni}$	SN Type
60 H[a]	4.25	2.70	0.21	1.38	0.17	(0.24)[b]	Ic???
20 He	3.55	2.00	0.24	0.65	0.09	0.13	Ib??
10 He	3.51	1.96	0.25	0.70	0.08	0.07–0.11	Ib??
7 He	3.20	1.70	0.40	0.44	0.07	0.08–0.15	Ib??
5 He	2.82	1.44	0.76	0.18	0.04	0.12	Ib??
4 He	2.26	0.91	0.64	0.05	0.02	0.07	Ib??
1.4 C/O[c]	...	1.40	0	0.13	0.15	0.63	Ia?

[a] From WLW.
[b] Uncertain; cf. WLW.
[c] From Thielemann et al. 1986.

TABLE 5

NUCLEAR REACTION NETWORK EMPLOYED

Element	A_{min}	A_{max}
H	1	3
He	3	4
Li	6	8
Be	7	9
B	8	11
C	11	14
N	13	15
O	15	18
F	17	19
Ne	19	23
Na	22	24
Mg	23	27
Al	25	28
Si	27	32
P	29	34
S	31	37
Cl	33	38
Ar	36	41
K	37	42
Ca	40	49
Sc	41	50
Ti	44	51
V	45	52
Cr	48	55
Mn	51	57
Fe	52	61
Co	55	62
Ni	56	65
Cu	57	66
Zn	60	69
Ga	61	70
Ge	64	71

1993). As we shall see, this had very little effect on the final presupernova star though it did increase its iron core mass by $\sim 0.1\ M_\odot$.

For all models except 7K the composition assumed for each zone at the link was given by what had been calculated by the Göttingen code, if the isotope had carried in that calculation, and solar otherwise (Anders & Grevesse 1989).

3.1. *Presupernova Models*

The presupernova models for stars that began as 4, 5, 7, 10, and 20 $M_\odot$ helium cores are given in Figures 6–11. The density profiles are given in Figure 6. In general, the density structures resemble those of helium cores of the same final mass evolved without mass loss. The structures would also be similar to the helium cores of massive stars evolved without mass loss provided the stars were chosen to have final helium cores of equivalent mass. Since our helium cores have converged on a final mass around 3 $M_\odot$, the equivalent star on the main sequence would have a mass of $\sim 12\ M_\odot$ (Weaver & Woosley 1995). As discussed in WLW, however, the compositions of our cores are different from any stars evolved without mass loss. A small-mass helium core evolved *with* mass loss would also be quite different. For helium cores starting with less than 4 $M_\odot$ and experiencing the same mass loss as parameterized here, the final configuration would have a degenerate core and a very thin helium shell. Such stars are not considered here because they would produce too little ^{56}Ni to be Type Ib supernovae.

The presupernova stars are very similar for the two 10 $M_\odot$ models evolved using differing treatments of semiconvection. The only noticeable difference is a larger iron core for the model evolved with greater semiconvective mixing (model 10S). This is a consequence of the electron capture that goes on during silicon shell burning and can be easily understood in the extreme limits of Ledoux and Schwarzschild convection. The latter examines only the temperature gradient and not the composition. Thus the fact that the electron mole number, Y_e, may be considerably smaller than 0.50 in the silicon-burning shell does not affect the convective decision, even though oxygen-rich material has Y_e very near 0.50. This means that the silicon convective region can grow without experiencing the barrier to buoyancy which really exists and of which the Ledoux criterion takes proper account. Since the mass of the

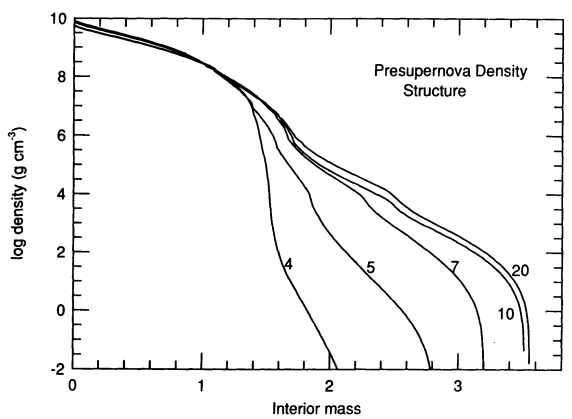

FIG. 6.—Density as a function of interior mass ($M_\odot$) in the final presupernova models. Note the convergence to a common structure in the inner 1.4 $M_\odot$. Models having steeper density declines outside this iron core will synthesize less heavy elements in the explosion and be characterized by higher velocities.

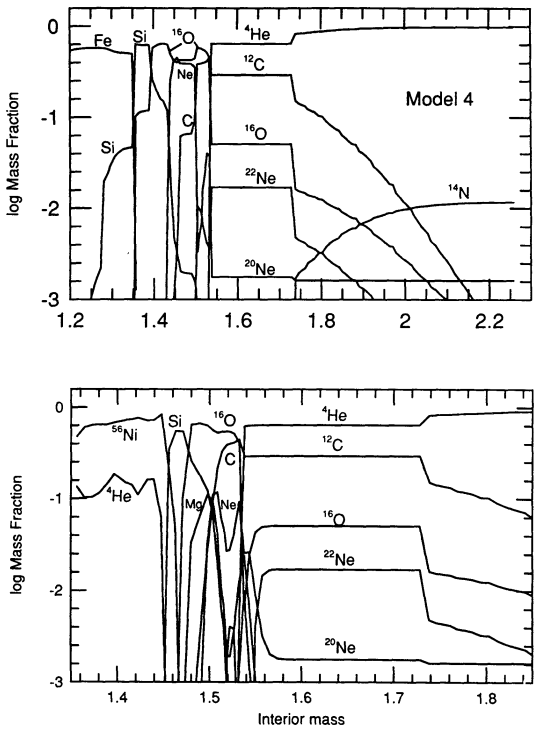

FIG. 7.—Composition of model 4 at the time of core collapse ($v_{collapse}$ first surpasses 1000 km s^{-1}; *upper panel*) and after the supernova (*lower panel*). In the presupernova plot, the inner neutronized iron core is not shown. In the lower panel the inner part of the ejecta that experiences substantial explosive processing has been expanded. Composition outside 1.85 $M_\odot$ in the lower panel is the same as before the explosion.

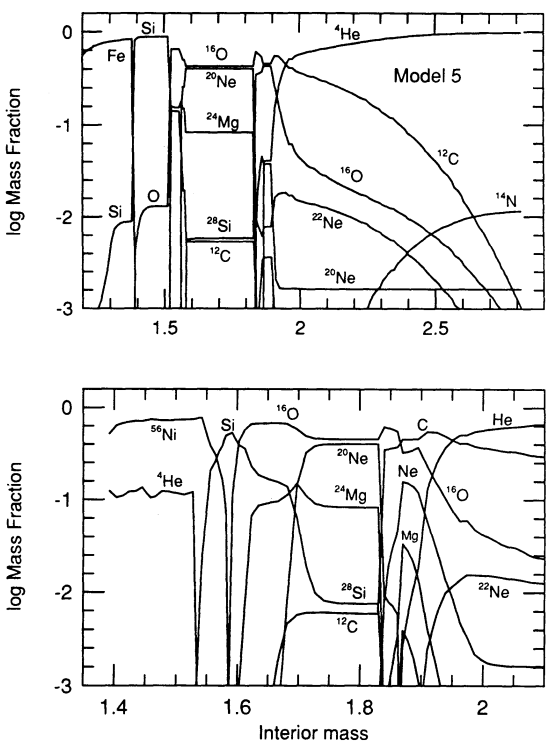

FIG. 8.—Presupernova and final composition of model 5 (see Fig. 7)

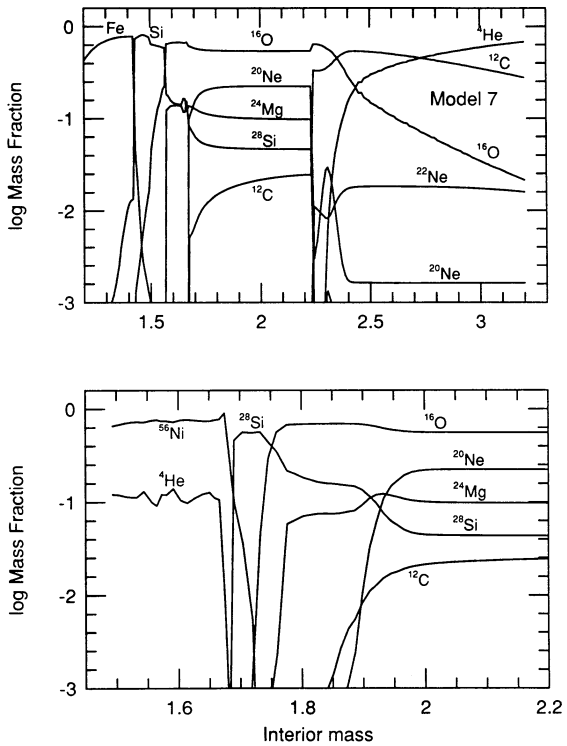

FIG. 9.—Presupernova and final composition of model 7A (see Fig. 7)

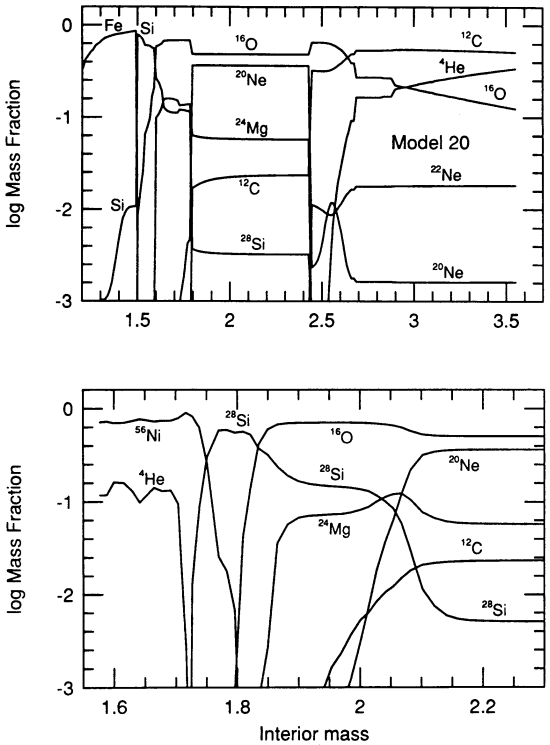

FIG. 11.—Presupernova and final composition for model 20 (see Fig. 7)

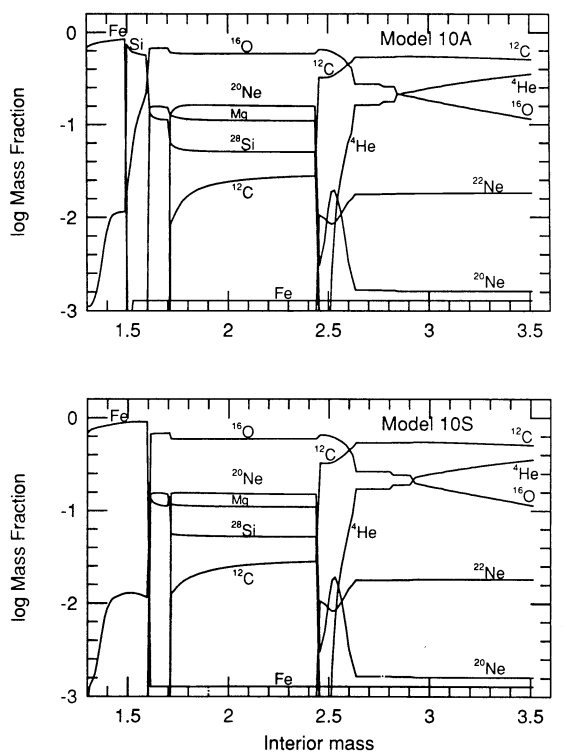

FIG. 10.—Presupernova abundances in models 10A and 10S. Both started from the same model at carbon ignition and both employed a Ledoux model for convection, but model 10S included a semiconvective diffusion coefficient 1000 times greater than 10A. Note the absence of a silicon shell in model 10S.

iron core is set by the maximum extent of the final episode of silicon shell burning, Schwarzschild-based calculations *can* (and in this case do) give larger iron cores for otherwise similar stars. To the extent that a semiconvective diffusion coefficient 1000 times greater makes the code more "Schwarzschild-like," a larger core results here. In fact, in model 10S the growth of the last silicon shell was only halted when it reached the large entropy increase associated with the oxygen shell.

Caution must be exercised in generalizing this result however. The size of the iron core is also sensitive to how many episodes of convective silicon shell burning there are. The first episode to extend outside the effective Chandrasekhar mass (as adjusted for finite entropy, Y_e gradient, boundary pressure, etc.) leads to collapse. Sometimes a very efficient first episode of silicon shell burning, or even silicon core burning, can lead to collapse with a *smaller* iron core. That was not the case here.

As mentioned earlier, a calibration run, model 7K, was calculated using the KEPLER code and the network in Table 5 for the complete evolution. This model was created by first extracting the inner 7 $M_\odot$ of a 25 $M_\odot$ star that had exhausted hydrogen in its center. The abundances in this core reflected the products of convective hydrogen burning in a massive star as calculated using a 200 isotope network. They were very nearly constant throughout. Some major abundances were, by mass: ^{4}He, 0.982; ^{12}C, 3.99×10^{-4}; ^{14}N, 0.0118, ^{16}O, 4.40×10^{-4}; ^{17}O, 2.48×10^{-5}; ^{18}O, 6.15×10^{-4}; ^{20}Ne, 0.00159; ^{22}Ne, 1.46×10^{-5}; ^{23}Na, 1.88×10^{-4}; and traces of heavier isotopes up through Ge. Since these abundances will later characterize the outer layers of the supernova, it is important that the products of the CNO tricycle and Ne-Na cycle properly reflect the fact that before the star was a helium star, it burned hydrogen. For example, the abundance of sodium is about 6 times solar, and this may have an appreciable effect upon the spectrum.

This 7 $M_\odot$ extract was relaxed into thermal and hydrostatic equilibrium with zero surface boundary pressure and allowed to resume its evolution. At helium ignition the radius was 6.3×10^{10} cm and the luminosity was 3.19×10^{38} ergs s^{-1}. These quantities agree well with the corresponding 7 $M_\odot$ model calculated in the Göttingen code. The model contained 540 zones at this point, each carrying its own 200 isotope network. This model was then evolved employing the same mass-loss prescription as for the other 7 $M_\odot$ models [$6 \times 10^{-8}(M/M_\odot)^{2.5}$ $M_\odot$ yr^{-1}]. At central helium depletion the mass of this model had declined to 3.92 $M_\odot$, somewhat larger than the equivalent model 7A (3.20 $M_\odot$). The difference was traced to the way in which semiconvection is treated in the two codes. The KEPLER code, operating in its "restrictive semiconvection" mode has even less semiconvection than the Göttingen code. Thus, in KEPLER, the extent of the helium-burning convective region became smaller as the core lost mass. This meant less helium was burned and, since the stars had similar luminosity, model 7K had a shorter lifetime and less mass loss.

The model was then recalculated in KEPLER using a larger mass-loss rate, $1 \times 10^{-7}(M/M_\odot)^{2.5}$ $M_\odot$ yr^{-1}, using otherwise identical physics. The final mass for model 7K was then 3.26 $M_\odot$, acceptably close to model 7A. Even so, the structure at helium depletion differed slightly. As a result of its slightly different mass and helium profile in the outer layers, a final stage of neon shell burning that occurred in model 7A did not occur in 7K. Details of abundances, both at carbon ignition and following the supernova explosion will be discussed in § 4.1. In the end, however, the nucleosynthesis of primary isotopes in models 7K and 7A were quite similar.

4. EXPLOSION

Explosion was simulated in all models using a piston (see also WLW). Table 6 gives its characteristics. The critical choice in parameterizing the explosion is the choice of where to put this piston. Obvious possibilities are the edge of the iron core, where a large change in Y_e is encountered, and the base of the oxygen shell, where there is a large jump in entropy, possibly facilitating the development of a mass separation. Here, in the general case, we located the piston at the edge of the iron core, but for the 7 and 10 $M_\odot$ models this location was varied. In each case, the piston was first moved smoothly inward, over a period of 0.45 s, from its starting radius to 500 km, and then given a sudden motion outward. The initial outward velocity of the piston at 500 km, the maximum radius to which it was moved, and the time it took to go that distance are given in Table 6. In all cases the trajectory of the piston between 0.45 s and its maximum radius was that of a projectile launched vertically with the given initial speed in a gravitational potential, $g(r)$, that remained $\frac{1}{2}$ of GM_{pist}/r^2. If the piston still had outward motion after 20.5 s, it was halted and held permanently stationary.

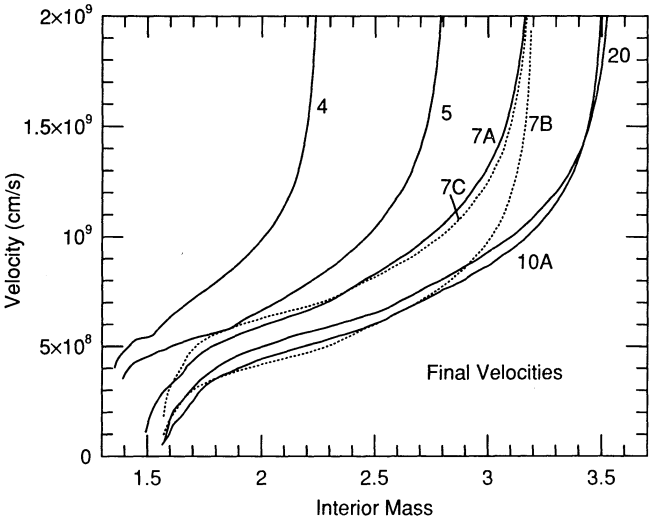

FIG. 12.—Final velocities after expansion has become homologous throughout the supernova ejecta.

The supersonic motion of the piston created an outward-moving shock which ejected most of the star external to the piston. The final kinetic energies of the ejecta when the internal energy had become negligible and expansion had become homologous (coasting) are also given in Table 6, and the final velocity profiles are given in Figure 12. In some cases, models 7A, 10A, and 20, the final mass separation did not correspond to the piston mass. This is because some matter fell back during the explosion. Details of this fallback, which occurs as the piston moves through regions of the mantle characterized by increasing ρr^3, have been discussed by Herant & Woosley (1994) and Woosley & Weaver (1995). To some extent this reduces the arbitrariness of the siting of the piston. Had pistons been placed deeper in the star or given less energy, more fallback would have occurred.

The shock wave also produces heating and explosive nucleosynthesis. Particularly critical to the light curve which follows is the production of ~ 0.1 $M_\odot$ of ^{56}Ni (Table 6). Also of interest are the masses of the final bound remnants which range from

TABLE 6

EXPLOSION CHARACTERISTICS OF ALL MODELS

Model	M_f ($M_\odot$)	$M_{C/O}$ ($M_\odot$)	M_{Fe} ($M_\odot$)	M_{pist} ($M_\odot$)	Remnant ($M_\odot$)	V_0 (10^4 km s^{-1})	R_{max} (10^4 km)	t_{stop} (s)	KE_∞ (10^{51} ergs)	$M_{^{56}Ni}$ ($M_\odot$)
4.....	2.26	1.53	1.35	1.35	1.35	2.00	14.1	20.5	0.85	0.070
5.....	2.82	1.87	1.38	1.38	1.38	1.95	9.63	20.5	1.19	0.124
7A.....	3.20	2.30	1.42	1.42	1.48	1.91	1.95	9.45	1.50	0.148
7B.....	3.20	2.30	1.42	1.57	1.57	2.01	2.26	11.5	0.76	0.079
7C.....	3.20	2.30	1.42	1.57	1.57	2.12	13.1	20.5	1.34	0.080
7K.....	3.26	2.30	1.38	1.38	1.38	2.00	12.6	20.5	1.10	0.077
10A.....	3.51	2.50	1.49	1.49	1.55	1.93	0.86	3.25	1.23	0.111
10B.....	3.51	2.50	1.49	1.59	1.59	2.10	10.2	20.5	1.27	0.070
10S.....	3.51	2.50	1.59	1.59	1.59	2.10	10.2	20.5	1.27	0.068
20.....	3.55	2.53	1.49	1.49	1.55	1.96	1.71	7.45	1.51	0.132

1.35 to 1.59 $M_\odot$ (baryonic mass). The neutron star gravitational masses would be 10%–15% smaller.

4.1. *Ejected Nucleosynthesis*

As §§ 2.1 and 2.2 described, for all models except 7K, nucleosynthesis calculations began on the helium-burning main sequence and used a small network to track reactions on isotopes up to and including silicon. The composition at helium depletion was then mapped into a 200 isotope network (Table 5) and evolved, including all convective coupling, in all zones through the remainder of the evolution and the supernova explosion. The neutrino process (Woosley et al. 1990) was included in the explosive nucleosynthesis calculation in all zones.

The final ejected abundances and their ratios normalized to solar (Anders & Grevesse 1989) values are given in Tables 7–9. Table 7 gives the production factors defined by the ratio of the mass fraction of the given isotope, after all weak decays have ended, to the mass fraction in the Sun. The reciprocal of this number is approximately the fraction of the solar nebula that would need to have experienced the sort of evolution in supernovae that we describe here in order to produce its correct abundance. Any detailed comparison requires an integral over masses and at least an approximate calculation of galactic chemical evolution (including, e.g., metallicity dependence in the nucleosynthesis). However, to the extent that the numbers in Table 7 are large and of similar value (for a given stellar mass), one can say that appreciable synthesis of many isotopes can occur in these stars. For example, model 7A has a production factor for ^{16}O of 26, but probably oxygen comes mainly from massive stars that do not experience so much mass loss (e.g., 25 $M_\odot$ single stars); carbon is bigger here, 77. It seems that, roughly speaking, other isotopes with production factors in the 20–60 range are coproduced in "acceptable" amounts. Much smaller values (e.g., for ^{13}C) suggest that the species is not made here, and much larger values signal problems in the calculation.

One such problem is ^{11}B, made here by the neutrino process. The temperature assumed for the μ- and τ-neutrinos, 8 MeV, was possibly too high. A more realistic value, $\sim$6 MeV, would bring ^{11}B down by a factor of 2, but would also reduce ^{19}F and ^{7}Li production. A somewhat larger value for ^{12}C(α, γ)^{16}O would reduce the carbon abundance (1.7 times Caughlan & Fowler 1988 was used here) and the boron which is made from it. More efficient convection late in helium burning could do the same thing. Recent measurements (Azuma et al. 1994) make it unlikely that the ^{12}C(α, γ)^{16}O reaction rate should be increased beyond what we used.

Another problem is ^{30}Si, but only in the 7 and 10 $M_\odot$ models. This probably reflects the inadequacy of the reaction network used during helium burning (see below), or the need to carry a finer grid of stellar masses in the nucleosynthesis study. Here ^{30}Si is chiefly the product of neon burning and is sensitive to how convection is treated in the shell-burning episodes.

There is also a general problem for the isotopes just above iron. The nuclei ^{57}Fe, ^{59}Co, ^{58}Ni, ^{60}Ni, ^{61}Ni, and ^{62}Ni are all overproduced. This problem often surfaces in lower mass supernovae ($\lesssim$15 $M_\odot$; Woosley & Weaver 1995). These species are made as ^{57}Ni, ^{58}Ni, ^{59}Cu, ^{60}Zn, ^{61}Zn, and ^{62}Zn, all in the α-rich freeze-out from nuclear statistical equilibrium in the innermost zones ejected by the supernovae. For lower mass helium cores, the fraction of material experiencing this kind of freeze-out is large compared to the yield of such standard elements as oxygen (more correctly, the latter is small). The situation is exacerbated here by lack of the "reverse shock" which ordinarily occurs in Type IIp supernovae when the expanding helium core runs into the hydrogen envelope. Because the deceleration is not present, more α-rich freeze-out escapes rather than falling back to the neutron star. In any case, these yields are most sensitive to the uncertain parameterization of the explosion, though several also have important *s*-process contributions.

Table 9 gives the nucleosynthesis in solar masses for all the important isotopes produced in these explosions (stable as well as radioactive progenitors) evaluated at a time when the supernova is 100 s old. At this point, explosive nucleosynthesis has ceased, but many unstable isotopes have not yet decayed. Of some interest are the abundances of ^{22}Na, ^{26}Al, ^{44}Ti, and ^{60}Fe, the last three especially being targets for gamma-ray astronomy. As do other supernovae in massive stars (Weaver & Woosley 1993; Woosley & Weaver 1995), these SN Ib models produce large amounts of each.

Because of their low final masses, these stars have their helium-burning shell relatively close to the stellar center (as compared to more massive stars without mass loss). Consequently a vigorous neutron irradiation can occur as the shock passes through and raises ^{22}Ne to high temperature. For the 4 $M_\odot$ model the helium shell was located at 1.5×10^9 cm; for the 20 $M_\odot$ model the shell was at 3×10^9 cm. The shock temperature and neutron mass fraction at the base of the helium shell in model 4 are shown as a function of time in Figure 13. The density at peak temperature was 4300 g cm^{-3}, and this declined approximately as T^3 following shock passage. The mass fraction of ^{22}Ne in this shell in the presupernova star was 0.017 and that of ^{4}He was 0.64, the remainder being chiefly ^{12}C (0.292) and ^{16}O (0.044). Following shock passage the ^{22}Ne had been completely burned to ^{25}Mg and ^{26}Mg and a number of elements (e.g., iron) had been forced into the most neutron-rich isotope carried in the network. It would be interesting to study such zones for their *r*-process characteristics. However, a short distance away in the same star, 0.02 $M_\odot$ farther out, the peak temperature only reached about 7×10^8 K and the maximum neutron mass fraction was

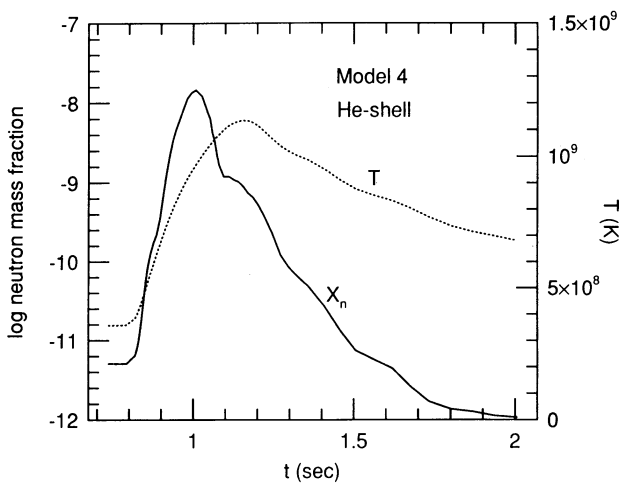

FIG. 13.—Neutron mass fraction (X_n) and temperature as the shock passes through the base of the helium layer during the explosion of model 4. This helium layer was unusually close to the neutron star. The density here was several thousand g cm^{-3} implying *r*-process conditions, albeit for a short time and in a very limited mass (see text).

TABLE 7

PRODUCTION FACTORS

Isotope	4	5	7A	7B	7C	10A	10S	20
^{4}He	2.55	1.92	.84	.88	.88	.46	.47	.43
^{7}Li	32.23	25.17	14.78	17.75	12.94	9.15	7.39	7.86
^{10}B	.12	.27	.04	.05	.05	.04	.04	.04
^{11}B	127.49	135.66	129.62	157.56	136.98	121.80	122.73	136.07
^{12}C	31.39	39.33	76.59	83.53	83.41	94.08	96.16	94.67
^{13}C	1.47	1.05	.65	.74	.70	.68	.70	.59
^{14}N	4.43	2.62	.00	.00	.00	.00	.00	.00
^{15}N	1.17	3.02	2.93	3.97	3.49	3.58	4.04	3.44
^{16}O	5.27	12.73	25.76	29.09	28.65	37.04	38.55	34.31
^{17}O	3.09	2.85	1.79	2.07	1.98	1.81	1.73	1.66
^{18}O	96.25	111.01	11.37	12.11	11.96	.01	.01	.01
^{19}F	11.16	27.77	20.36	33.01	27.81	19.89	21.66	46.52
^{20}Ne	2.92	27.01	28.24	33.02	32.57	27.23	28.28	46.03
^{21}Ne	8.03	34.80	25.13	21.01	30.31	15.42	9.87	48.54
^{22}Ne	31.16	30.49	61.53	73.50	69.94	69.90	72.65	63.13
^{23}Na	2.35	22.21	20.74	27.81	25.90	21.30	21.67	49.70
^{24}Mg	7.04	29.56	49.96	57.61	56.51	68.24	73.00	40.25
^{25}Mg	7.13	30.68	38.99	39.29	41.89	38.53	41.03	55.19
^{26}Mg	8.62	23.33	29.14	27.51	29.91	28.31	30.30	41.70
^{27}Al	6.80	26.64	50.69	60.73	58.68	70.57	78.18	43.73
^{28}Si	29.07	43.11	71.06	65.12	70.64	66.06	61.94	68.85
^{29}Si	11.92	19.96	52.32	59.54	58.37	74.58	85.26	31.74
^{30}Si	24.05	55.03	121.12	123.65	126.43	142.48	151.54	84.90
^{31}P	16.60	27.46	73.35	80.48	80.25	89.67	97.14	50.56
^{32}S	19.31	26.24	32.33	26.45	29.95	27.17	24.05	37.62
^{33}S	12.25	18.84	28.79	28.95	29.43	27.35	22.80	32.26
^{34}S	16.26	36.90	56.34	52.42	55.80	49.90	45.51	53.25
^{36}S	19.01	26.60	58.72	56.27	60.93	51.46	58.15	38.49
^{35}Cl	12.78	16.85	39.00	44.21	45.49	40.16	39.01	31.39
^{37}Cl	7.68	14.11	17.25	19.14	19.91	17.12	16.51	21.91
^{36}Ar	16.71	26.25	22.40	18.05	19.85	20.07	20.09	28.37
^{38}Ar	4.77	14.36	15.31	18.93	19.73	17.95	10.83	17.56
^{40}Ar	27.60	48.43	60.17	39.40	53.63	33.40	28.14	66.67
^{39}K	5.69	7.73	9.11	8.91	10.20	7.92	7.39	9.42
^{40}K	13.43	20.25	36.07	46.04	43.25	43.91	46.47	32.49
^{41}K	7.65	8.25	9.93	8.14	9.49	7.47	7.40	9.74
^{40}Ca	16.84	33.89	19.39	17.02	17.62	20.44	23.21	28.37
^{42}Ca	6.51	13.78	14.54	17.01	18.46	16.91	11.11	16.17
^{43}Ca	6.92	8.86	11.70	7.63	7.84	7.71	7.45	7.45
^{44}Ca	27.64	29.44	34.21	24.70	30.37	23.41	26.33	26.03
^{46}Ca	17.86	40.81	51.52	26.91	44.46	23.70	16.89	52.31
^{48}Ca	1.06	.91	.89	.71	.81	.66	.68	.93
^{45}Sc	20.58	29.54	41.65	29.24	18.55	33.87	15.42	25.99
^{46}Ti	14.82	19.00	21.19	17.99	22.03	19.21	14.67	18.84
^{47}Ti	4.84	6.12	7.38	5.76	5.95	5.34	5.43	5.64
^{48}Ti	39.45	51.98	45.01	33.90	39.08	34.48	39.15	39.64
^{49}Ti	23.35	37.85	24.58	20.97	23.06	23.66	27.14	27.33
^{50}Ti	2.03	3.64	4.48	5.09	5.12	4.99	5.00	5.17
^{50}V	11.14	13.54	32.92	39.19	37.29	45.91	51.99	22.82
^{51}V	12.43	28.78	13.22	14.95	14.89	16.82	17.69	22.72
^{50}Cr	21.71	30.78	33.02	26.61	30.48	25.26	24.83	43.06
^{52}Cr	18.45	57.88	15.41	21.30	21.38	26.60	30.79	36.74
^{53}Cr	18.30	51.91	16.87	21.32	21.32	25.14	28.98	35.09
^{54}Cr	3.42	6.85	7.73	9.43	8.88	9.28	9.98	9.53
^{55}Mn	17.81	35.63	23.40	19.79	15.41	20.42	17.38	25.66
^{54}Fe	16.21	32.73	24.39	21.68	21.87	22.05	22.57	35.41
^{56}Fe	66.47	75.02	87.12	42.17	42.77	49.12	30.92	57.44
^{57}Fe	158.40	151.64	201.10	80.45	84.23	92.81	63.80	100.95
^{58}Fe	11.28	26.20	40.15	43.57	42.89	46.61	48.48	42.24
^{59}Co	100.61	109.15	164.88	73.27	69.36	74.93	51.92	80.41
^{58}Ni	216.01	193.89	323.46	69.54	72.74	79.66	51.42	87.47
^{60}Ni	121.40	116.28	151.07	71.79	79.27	86.10	53.10	88.25
^{61}Ni	258.35	252.43	348.46	146.25	163.86	162.77	113.39	182.83
^{62}Ni	608.82	567.55	859.40	227.82	241.88	262.94	177.00	259.66
^{64}Ni	21.65	28.19	32.57	39.99	38.17	34.90	30.47	36.26
^{63}Cu	28.16	38.01	51.93	42.71	37.66	40.23	35.92	38.72
^{65}Cu	45.72	57.51	73.48	46.17	64.53	31.04	20.19	82.39
^{64}Zn	16.07	14.42	18.62	10.22	10.83	11.53	7.96	12.17
^{66}Zn	66.63	66.38	89.67	32.84	34.70	34.26	25.97	36.05
^{67}Zn	5.40	11.67	11.89	14.37	13.34	10.36	11.17	11.53
^{68}Zn	8.97	12.37	13.19	16.40	15.27	13.10	14.31	12.10
^{70}Zn	27.07	21.02	16.84	16.74	18.05	12.29	12.02	20.18
^{69}Ga	74.81	82.47	74.42	55.90	72.45	40.50	25.74	87.45
^{71}Ga	71.12	108.57	83.00	101.91	96.92	72.31	100.98	74.05
^{70}Ge	8.33	19.86	19.88	22.33	22.15	14.36	17.43	17.12

TABLE 8

FINAL YIELDS (in $M_\odot$)

Isotope	4	5	7A	7B	7C	10A	10S	20
^{4}He	6.40E-01	7.56E-01	4.06E-01	3.95E-01	3.94E-01	2.49E-01	2.47E-01	2.36E-01
^{7}Li	2.74E-07	3.37E-07	2.38E-07	2.70E-07	1.96E-07	1.67E-07	1.33E-07	1.46E-07
^{11}B	5.49E-07	9.19E-07	1.09E-06	1.21E-06	1.05E-06	1.13E-06	1.11E-06	1.28E-06
^{12}C	8.66E-02	1.71E-01	4.12E-01	4.12E-01	4.11E-01	5.58E-01	5.59E-01	5.69E-01
^{13}C	4.89E-05	5.48E-05	4.20E-05	4.37E-05	4.18E-05	4.88E-05	4.93E-05	4.29E-05
^{14}N	4.45E-03	4.15E-03	5.42E-06	6.46E-06	5.83E-06	5.78E-06	6.24E-06	6.56E-06
^{15}N	4.66E-06	1.89E-05	2.27E-05	2.82E-05	2.47E-05	3.06E-05	3.38E-05	2.98E-05
^{16}O	4.60E-02	1.75E-01	4.39E-01	4.54E-01	4.46E-01	6.95E-01	7.09E-01	6.53E-01
^{17}O	1.09E-05	1.59E-05	1.23E-05	1.31E-05	1.25E-05	1.37E-05	1.29E-05	1.28E-05
^{18}O	1.90E-03	3.45E-03	4.37E-04	4.27E-04	4.21E-04	5.15E-07	5.53E-07	5.43E-07
^{19}F	4.11E-06	1.61E-05	1.46E-05	2.17E-05	1.83E-05	1.58E-05	1.68E-05	3.74E-05
^{20}Ne	4.30E-03	6.27E-02	8.12E-02	8.69E-02	8.56E-02	8.63E-02	8.78E-02	1.48E-01
^{21}Ne	3.02E-05	2.06E-04	1.84E-04	1.41E-04	2.03E-04	1.24E-04	7.82E-05	3.97E-04
^{22}Ne	3.69E-03	5.69E-03	1.42E-02	1.56E-02	1.48E-02	1.78E-02	1.81E-02	1.63E-02
^{23}Na	7.14E-05	1.06E-03	1.23E-03	1.51E-03	1.40E-03	1.39E-03	1.39E-03	3.29E-03
^{24}Mg	3.30E-03	2.18E-02	4.57E-02	4.82E-02	4.72E-02	6.88E-02	7.21E-02	4.11E-02
^{25}Mg	4.39E-04	2.97E-03	4.68E-03	4.32E-03	4.60E-03	5.10E-03	5.32E-03	7.41E-03
^{26}Mg	6.08E-04	2.59E-03	4.01E-03	3.47E-03	3.77E-03	4.30E-03	4.51E-03	6.42E-03
^{27}Al	3.59E-04	2.21E-03	5.22E-03	5.73E-03	5.53E-03	8.02E-03	8.70E-03	5.04E-03
^{28}Si	1.73E-02	4.03E-02	8.24E-02	6.91E-02	7.49E-02	8.44E-02	7.76E-02	8.92E-02
^{29}Si	3.71E-04	9.80E-04	3.18E-03	3.32E-03	3.25E-03	5.00E-03	5.60E-03	2.16E-03
^{30}Si	5.15E-04	1.85E-03	5.06E-03	4.73E-03	4.83E-03	6.56E-03	6.83E-03	3.96E-03
^{31}P	1.23E-04	3.21E-04	1.06E-03	1.07E-03	1.06E-03	1.43E-03	1.52E-03	8.18E-04
^{32}S	6.95E-03	1.49E-02	2.27E-02	1.70E-02	1.92E-02	2.10E-02	1.82E-02	2.95E-02
^{33}S	3.59E-05	8.70E-05	1.64E-04	1.52E-04	1.54E-04	1.72E-04	1.41E-04	2.06E-04
^{34}S	2.76E-04	9.86E-04	1.87E-03	1.59E-03	1.69E-03	1.82E-03	1.63E-03	1.97E-03
^{36}S	1.62E-06	3.57E-06	9.78E-06	8.58E-06	9.28E-06	9.45E-06	1.05E-05	7.16E-06
^{35}Cl	2.94E-05	6.11E-05	1.75E-04	1.82E-04	1.87E-04	1.99E-04	1.89E-04	1.58E-04
^{37}Cl	5.97E-06	1.73E-05	2.61E-05	2.66E-05	2.76E-05	2.86E-05	2.71E-05	3.71E-05
^{36}Ar	1.18E-03	2.91E-03	3.08E-03	2.27E-03	2.49E-03	3.04E-03	2.98E-03	4.36E-03
^{38}Ar	6.67E-05	3.16E-04	4.18E-04	4.73E-04	4.93E-04	5.40E-04	3.20E-04	5.36E-04
^{40}Ar	6.35E-07	1.75E-06	2.70E-06	1.62E-06	2.20E-06	1.65E-06	1.37E-06	3.34E-06
^{39}K	1.80E-05	3.85E-05	5.40E-05	5.03E-05	5.75E-05	5.38E-05	4.92E-05	6.49E-05
^{40}K	6.77E-08	1.61E-07	3.55E-07	4.15E-07	3.89E-07	4.77E-07	4.94E-07	3.57E-07
^{41}K	1.83E-06	3.11E-06	4.46E-06	3.49E-06	4.06E-06	3.85E-06	3.74E-06	5.09E-06
^{40}Ca	9.17E-04	2.91E-03	2.05E-03	1.66E-03	1.71E-03	2.40E-03	2.67E-03	3.37E-03
^{42}Ca	2.48E-06	8.28E-06	1.06E-05	1.16E-05	1.26E-05	1.39E-05	8.94E-06	1.35E-05
^{43}Ca	5.65E-07	1.14E-06	1.52E-06	1.11E-06	1.14E-06	1.35E-06	1.28E-06	1.33E-06
^{44}Ca	3.58E-05	6.01E-05	7.74E-05	5.72E-05	7.03E-05	6.53E-05	7.20E-05	7.36E-05
^{46}Ca	4.54E-08	1.63E-07	2.55E-07	1.22E-07	2.02E-07	1.29E-07	9.05E-08	2.90E-07
^{48}Ca	1.33E-07	1.80E-07	2.19E-07	1.60E-07	1.83E-07	1.78E-07	1.79E-07	2.57E-07
^{45}Sc	7.29E-07	1.65E-06	2.39E-06	1.85E-06	1.17E-06	2.58E-06	1.15E-06	2.01E-06
^{46}Ti	3.01E-06	6.08E-06	7.95E-06	6.53E-06	7.99E-06	8.40E-06	6.28E-06	8.35E-06
^{47}Ti	9.16E-07	1.82E-06	2.37E-06	1.95E-06	2.01E-06	2.17E-06	2.17E-06	2.33E-06
^{48}Ti	7.71E-05	1.60E-04	1.56E-04	1.18E-04	1.36E-04	1.45E-04	1.61E-04	1.69E-04
^{49}Ti	3.48E-06	8.87E-06	6.67E-06	5.58E-06	6.13E-06	7.58E-06	8.51E-06	8.87E-06
^{50}Ti	3.04E-07	8.56E-07	1.31E-06	1.36E-06	1.37E-06	1.61E-06	1.58E-06	1.69E-06
^{50}V	9.38E-09	1.80E-08	5.41E-08	5.90E-08	5.61E-08	8.32E-08	9.23E-08	4.19E-08
^{51}V	4.26E-06	1.55E-05	8.54E-06	9.15E-06	9.11E-06	1.24E-05	1.28E-05	1.70E-05
^{50}Cr	1.47E-05	3.27E-05	4.35E-05	3.21E-05	3.67E-05	3.67E-05	3.54E-05	6.34E-05
^{52}Cr	2.49E-04	1.23E-03	3.84E-04	5.15E-04	5.16E-04	7.74E-04	8.77E-04	1.08E-03
^{53}Cr	2.86E-05	1.28E-04	5.05E-05	5.95E-05	5.94E-05	8.44E-05	9.54E-05	1.19E-04
^{54}Cr	1.35E-06	4.27E-06	5.97E-06	6.68E-06	6.28E-06	7.91E-06	8.34E-06	8.24E-06
^{55}Mn	2.15E-04	6.78E-04	4.37E-04	4.28E-04	3.33E-04	5.31E-04	4.43E-04	6.76E-04
^{54}Fe	1.05E-03	3.34E-03	3.08E-03	2.51E-03	2.53E-03	3.08E-03	3.09E-03	5.01E-03
^{56}Fe	7.07E-02	1.26E-01	1.49E-01	8.02E-02	8.12E-02	1.12E-01	6.93E-02	1.33E-01
^{57}Fe	4.11E-03	6.20E-03	7.44E-03	3.74E-03	3.90E-03	5.19E-03	3.49E-03	5.72E-03
^{58}Fe	3.80E-05	1.39E-04	2.45E-04	2.62E-04	2.57E-04	3.37E-04	3.44E-04	3.10E-04
^{59}Co	3.07E-04	5.25E-04	6.58E-04	4.00E-04	3.78E-04	4.92E-04	3.34E-04	5.35E-04
^{58}Ni	9.71E-03	1.37E-02	1.38E-02	5.59E-03	5.84E-03	7.71E-03	4.87E-03	8.58E-03
^{60}Ni	2.16E-03	3.26E-03	4.49E-03	2.29E-03	2.52E-03	3.30E-03	1.99E-03	3.43E-03
^{61}Ni	2.02E-04	3.11E-04	4.03E-04	2.04E-04	2.29E-04	2.74E-04	1.87E-04	3.12E-04
^{62}Ni	1.54E-03	2.26E-03	2.31E-03	1.03E-03	1.09E-03	1.43E-03	9.42E-04	1.43E-03
^{64}Ni	1.43E-05	2.94E-05	4.20E-05	4.73E-05	4.50E-05	4.97E-05	4.25E-05	5.23E-05
^{63}Cu	1.47E-05	3.13E-05	3.98E-05	4.00E-05	3.52E-05	4.53E-05	3.96E-05	4.42E-05
^{65}Cu	1.10E-05	2.18E-05	3.35E-05	1.99E-05	2.77E-05	1.61E-05	1.03E-05	4.33E-05
^{64}Zn	1.45E-05	2.05E-05	2.88E-05	1.65E-05	1.75E-05	2.24E-05	1.52E-05	2.39E-05
^{66}Zn	3.56E-05	5.59E-05	5.81E-05	3.14E-05	3.31E-05	3.94E-05	2.93E-05	4.20E-05
^{67}Zn	4.31E-07	1.46E-06	1.76E-06	2.05E-06	1.90E-06	1.78E-06	1.88E-06	2.00E-06
^{68}Zn	3.31E-06	7.19E-06	9.43E-06	1.08E-05	1.01E-05	1.04E-05	1.11E-05	9.74E-06
^{70}Zn	3.30E-07	4.03E-07	4.00E-07	3.65E-07	3.93E-07	3.22E-07	3.09E-07	5.36E-07
^{69}Ga	2.70E-06	4.68E-06	5.23E-06	3.60E-06	4.66E-06	3.14E-06	1.96E-06	6.87E-06
^{71}Ga	1.70E-06	4.09E-06	3.88E-06	4.36E-06	4.14E-06	3.72E-06	5.09E-06	3.86E-06
^{70}Ge	3.27E-07	1.23E-06	1.52E-06	1.57E-06	1.55E-06	1.21E-06	1.44E-06	1.47E-06
Total	9.10E-01	1.43E+00	1.72E+00	1.63E+00	1.62E+00	1.96E+00	1.92E+00	1.98E+00

TABLE 9

ISOTOPIC ABUNDANCES (in $M_\odot$) AT 200 s

Isotope	4	5	7A	7B	7C	10A	10S	20
^{4}He	6.40E-01	7.57E-01	4.07E-01	4.00E-01	4.01E-01	2.49E-01	2.47E-01	2.36E-01
^{7}Li	1.19E-07	1.39E-07	7.66E-08	9.16E-08	7.73E-08	4.53E-08	4.43E-08	3.80E-08
^{7}Be	1.55E-07	1.99E-07	1.61E-07	1.78E-07	1.19E-07	1.22E-07	8.82E-08	1.08E-07
^{10}B	1.20E-10	4.13E-10	8.05E-11	8.05E-11	8.10E-11	7.84E-11	7.88E-11	8.43E-11
^{11}B	3.16E-07	6.58E-07	6.27E-07	6.54E-07	5.80E-07	5.19E-07	4.98E-07	6.41E-07
^{11}C	2.33E-07	2.61E-07	4.61E-07	5.58E-07	4.73E-07	6.09E-07	6.16E-07	6.36E-07
^{12}C	8.66E-02	1.71E-01	4.13E-01	4.14E-01	4.13E-01	5.58E-01	5.59E-01	5.69E-01
^{13}C	4.79E-05	5.34E-05	3.80E-05	3.90E-05	3.77E-05	4.21E-05	4.23E-05	3.69E-05
^{14}C	3.71E-07	1.20E-06	5.09E-07	5.58E-07	5.36E-07	4.86E-07	4.23E-07	6.44E-07
^{13}N	9.85E-07	1.37E-06	4.19E-06	5.47E-06	4.98E-06	6.71E-06	6.95E-06	6.03E-06
^{14}N	4.45E-03	4.15E-03	4.92E-06	5.92E-06	5.32E-06	5.30E-06	5.81E-06	5.92E-06
^{15}N	4.05E-06	1.65E-05	1.80E-05	2.19E-05	1.53E-05	2.37E-05	2.61E-05	2.45E-05
^{15}O	6.15E-07	2.38E-06	4.69E-06	6.25E-06	9.38E-06	6.87E-06	7.70E-06	5.32E-06
^{16}O	4.60E-02	1.75E-01	4.39E-01	4.54E-01	4.46E-01	6.95E-01	7.09E-01	6.53E-01
^{17}O	1.09E-05	1.59E-05	1.24E-05	1.33E-05	1.27E-05	1.37E-05	1.29E-05	1.28E-05
^{18}O	1.90E-03	3.45E-03	4.41E-04	4.43E-04	4.42E-04	3.78E-07	3.93E-07	3.63E-07
^{19}F	4.11E-06	1.61E-05	1.46E-05	2.17E-05	1.83E-05	1.58E-05	1.68E-05	3.74E-05
^{20}Ne	4.30E-03	6.27E-02	8.12E-02	8.69E-02	8.56E-02	8.63E-02	8.78E-02	1.48E-01
^{21}Ne	3.02E-05	2.06E-04	1.84E-04	1.41E-04	2.03E-04	1.24E-04	7.82E-05	3.97E-04
^{22}Ne	3.69E-03	5.69E-03	1.43E-02	1.57E-02	1.49E-02	1.78E-02	1.81E-02	1.63E-02
^{22}Na	2.46E-08	6.01E-07	8.74E-07	1.18E-06	1.06E-06	1.02E-06	1.07E-06	1.69E-06
^{23}Na	7.13E-05	1.06E-03	1.23E-03	1.51E-03	1.40E-03	1.39E-03	1.39E-03	3.29E-03
^{24}Mg	3.29E-03	2.18E-02	4.57E-02	4.82E-02	4.72E-02	6.87E-02	7.21E-02	4.11E-02
^{25}Mg	4.39E-04	2.97E-03	4.68E-03	4.32E-03	4.60E-03	5.10E-03	5.32E-03	7.41E-03
^{26}Mg	6.03E-04	2.57E-03	3.96E-03	3.42E-03	3.72E-03	4.24E-03	4.43E-03	6.37E-03
^{26}Al	4.90E-06	2.41E-05	5.09E-05	5.50E-05	5.26E-05	6.23E-05	8.39E-05	4.28E-05
^{27}Al	3.56E-04	2.21E-03	5.21E-03	5.73E-03	5.52E-03	8.01E-03	8.70E-03	5.02E-03
^{28}Si	1.73E-02	4.03E-02	8.24E-02	6.91E-02	7.49E-02	8.44E-02	7.76E-02	8.92E-02
^{29}Si	3.71E-04	9.80E-04	3.18E-03	3.32E-03	3.25E-03	5.00E-03	5.60E-03	2.16E-03
^{30}Si	5.14E-04	1.85E-03	5.05E-03	4.72E-03	4.82E-03	6.55E-03	6.83E-03	3.96E-03
^{31}Si	1.15E-05	3.03E-05	6.44E-05	3.45E-05	5.05E-05	3.87E-05	3.33E-05	6.88E-05
^{31}P	1.12E-04	2.91E-04	9.97E-04	1.03E-03	1.01E-03	1.39E-03	1.49E-03	7.49E-04
^{32}S	6.94E-03	1.49E-02	2.27E-02	1.70E-02	1.92E-02	2.10E-02	1.82E-02	2.95E-02
^{33}S	3.56E-05	8.58E-05	1.61E-04	1.50E-04	1.52E-04	1.70E-04	1.39E-04	2.03E-04
^{34}S	2.76E-04	9.86E-04	1.87E-03	1.59E-03	1.69E-03	1.82E-03	1.63E-03	1.97E-03
^{35}S	8.48E-07	2.76E-06	1.01E-05	9.34E-06	9.93E-06	9.28E-06	9.94E-06	5.48E-06
^{36}S	1.62E-06	3.56E-06	9.73E-06	8.53E-06	9.23E-06	9.39E-06	1.04E-05	7.13E-06
^{35}Cl	2.86E-05	5.84E-05	1.65E-04	1.73E-04	1.77E-04	1.90E-04	1.79E-04	1.52E-04
^{36}Cl	2.22E-07	5.82E-07	2.30E-06	2.52E-06	2.44E-06	2.70E-06	2.78E-06	1.43E-06
^{37}Cl	3.97E-06	1.26E-05	1.88E-05	1.93E-05	1.94E-05	2.11E-05	2.13E-05	2.76E-05
^{36}Ar	1.18E-03	2.91E-03	3.07E-03	2.27E-03	2.49E-03	3.04E-03	2.98E-03	4.35E-03
^{37}Ar	1.95E-06	4.63E-06	7.27E-06	7.24E-06	8.15E-06	7.52E-06	5.80E-06	9.44E-06
^{38}Ar	6.58E-05	3.15E-04	4.15E-04	4.72E-04	4.91E-04	5.39E-04	3.19E-04	5.32E-04
^{39}Ar	5.56E-07	2.02E-06	2.78E-06	2.18E-06	2.58E-06	2.31E-06	1.91E-06	3.93E-06
^{40}Ar	6.28E-07	1.74E-06	2.66E-06	1.58E-06	2.16E-06	1.60E-06	1.31E-06	3.31E-06
^{41}Ar	2.80E-07	3.65E-07	7.08E-07	1.27E-07	3.86E-07	9.06E-08	3.18E-08	7.60E-07
^{39}K	1.74E-05	3.64E-05	5.12E-05	4.81E-05	5.49E-05	5.15E-05	4.73E-05	6.09E-05
^{40}K	6.77E-08	1.61E-07	3.55E-07	4.15E-07	3.89E-07	4.77E-07	4.94E-07	3.57E-07
^{41}K	2.54E-07	4.38E-07	5.23E-07	5.81E-07	5.53E-07	6.59E-07	6.76E-07	6.81E-07
^{40}Ca	9.17E-04	2.91E-03	2.05E-03	1.66E-03	1.71E-03	2.39E-03	2.67E-03	3.37E-03
^{41}Ca	1.30E-06	2.31E-06	3.23E-06	2.78E-06	3.12E-06	3.10E-06	3.03E-06	3.65E-06
^{42}Ca	2.39E-06	8.02E-06	1.02E-05	1.14E-05	1.23E-05	1.37E-05	8.82E-06	1.30E-05
^{43}Ca	1.09E-07	2.14E-07	3.05E-07	3.49E-07	3.27E-07	4.08E-07	4.13E-07	3.71E-07
^{44}Ca	1.07E-06	1.58E-06	1.71E-06	1.87E-06	1.80E-06	2.16E-06	2.21E-06	2.04E-06
^{45}Ca	3.65E-08	1.69E-07	2.34E-07	1.84E-07	2.23E-07	2.14E-07	1.68E-07	3.03E-07
^{46}Ca	4.54E-08	1.63E-07	2.55E-07	1.22E-07	2.02E-07	1.29E-07	9.05E-08	2.90E-07
^{47}Ca	2.35E-08	6.27E-08	1.10E-07	2.41E-08	6.74E-08	1.80E-08	7.04E-09	1.19E-07
^{48}Ca	1.33E-07	1.80E-07	2.19E-07	1.61E-07	1.84E-07	1.78E-07	1.79E-07	2.57E-07
^{43}Sc	4.56E-07	9.25E-07	1.22E-06	7.65E-07	8.16E-07	9.46E-07	8.70E-07	9.55E-07
^{44}Sc	8.31E-09	1.29E-08	1.71E-08	1.50E-08	1.21E-08	1.51E-08	1.31E-08	1.54E-08
^{45}Sc	6.10E-08	9.60E-08	1.69E-07	1.80E-07	1.58E-07	2.35E-07	2.30E-07	1.63E-07
^{46}Sc	7.37E-09	1.21E-08	4.05E-08	4.71E-08	4.39E-08	6.54E-08	7.39E-08	3.03E-08
^{47}Sc	6.08E-09	3.87E-09	1.53E-08	1.83E-08	1.69E-08	3.06E-08	3.63E-08	8.95E-09
^{44}Ti	3.48E-05	5.85E-05	7.57E-05	5.53E-05	6.85E-05	6.31E-05	6.97E-05	7.15E-05
^{45}Ti	6.31E-07	1.38E-06	1.98E-06	1.49E-06	7.92E-07	2.13E-06	7.54E-07	1.54E-06
^{46}Ti	3.01E-06	6.07E-06	7.91E-06	6.49E-06	7.95E-06	8.33E-06	6.21E-06	8.32E-06
^{47}Ti	2.14E-07	3.85E-07	4.88E-07	5.19E-07	4.39E-07	5.84E-07	5.35E-07	5.57E-07
^{48}Ti	1.42E-06	1.80E-06	1.68E-06	1.81E-06	1.72E-06	2.04E-06	2.08E-06	1.82E-06
^{49}Ti	2.44E-07	4.30E-07	6.16E-07	7.29E-07	6.77E-07	9.27E-07	1.02E-06	8.26E-07
^{50}Ti	3.03E-07	8.56E-07	1.31E-06	1.36E-06	1.37E-06	1.61E-06	1.58E-06	1.68E-06
^{51}Ti	5.36E-08	1.34E-07	2.25E-07	7.75E-08	1.92E-07	7.12E-08	3.01E-08	2.78E-07

TABLE 9—*Continued*

Isotope	4	5	7A	7B	7C	10A	10S	20
^{47}V	6.72E-07	1.37E-06	1.76E-06	1.39E-06	1.49E-06	1.54E-06	1.59E-06	1.64E-06
^{48}V	2.13E-07	4.29E-07	4.59E-07	3.97E-07	2.79E-07	4.39E-07	4.71E-07	5.08E-07
^{49}V	2.09E-07	5.18E-07	4.91E-07	4.33E-07	3.22E-07	5.50E-07	5.85E-07	6.46E-07
^{50}V	9.38E-09	1.80E-08	5.41E-08	5.90E-08	5.61E-08	8.32E-08	9.23E-08	4.19E-08
^{51}V	3.13E-07	4.57E-07	5.60E-07	5.39E-07	5.18E-07	6.24E-07	6.35E-07	6.38E-07
^{48}Cr	7.55E-05	1.58E-04	1.53E-04	1.16E-04	1.34E-04	1.42E-04	1.59E-04	1.67E-04
^{49}Cr	3.01E-06	7.91E-06	5.54E-06	4.41E-06	5.12E-06	6.09E-06	6.90E-06	7.37E-06
^{50}Cr	1.47E-05	3.27E-05	4.35E-05	3.21E-05	3.67E-05	3.67E-05	3.54E-05	6.34E-05
^{51}Cr	4.43E-07	1.34E-06	1.29E-06	1.28E-06	1.30E-06	1.41E-06	1.34E-06	2.05E-06
^{52}Cr	1.35E-05	2.65E-05	2.94E-05	2.55E-05	3.42E-05	2.94E-05	3.05E-05	3.40E-05
^{53}Cr	1.26E-06	1.73E-06	1.88E-06	2.12E-06	2.01E-06	2.60E-06	2.82E-06	2.22E-06
^{54}Cr	9.71E-07	2.95E-06	4.69E-06	5.10E-06	5.02E-06	6.42E-06	6.68E-06	6.06E-06
^{51}Mn	3.45E-06	1.36E-05	6.47E-06	7.26E-06	7.10E-06	1.03E-05	1.08E-05	1.40E-05
^{52}Mn	2.06E-06	8.29E-06	4.00E-06	4.79E-06	3.59E-06	6.53E-06	7.01E-06	8.81E-06
^{53}Mn	9.05E-06	3.54E-05	1.92E-05	1.99E-05	1.65E-05	2.54E-05	2.85E-05	3.89E-05
^{54}Mn	3.83E-07	1.33E-06	1.28E-06	1.59E-06	1.27E-06	1.50E-06	1.67E-06	2.18E-06
^{55}Mn	9.70E-06	1.35E-05	1.51E-05	1.67E-05	1.54E-05	2.00E-05	2.17E-05	1.77E-05
^{52}Fe	2.34E-04	1.20E-03	3.50E-04	4.84E-04	4.78E-04	7.38E-04	8.40E-04	1.04E-03
^{53}Fe	1.82E-05	9.05E-05	2.95E-05	3.74E-05	4.09E-05	5.64E-05	6.40E-05	7.84E-05
^{54}Fe	1.05E-03	3.34E-03	3.08E-03	2.51E-03	2.53E-03	3.08E-03	3.09E-03	5.01E-03
^{55}Fe	2.13E-05	3.72E-05	5.35E-05	3.97E-05	4.32E-05	3.97E-05	3.67E-05	6.22E-05
^{56}Fe	8.05E-04	1.04E-03	1.03E-03	1.08E-03	1.09E-03	1.29E-03	1.35E-03	1.15E-03
^{57}Fe	4.59E-05	9.27E-05	1.46E-04	1.67E-04	1.58E-04	2.26E-04	2.52E-04	1.89E-04
^{58}Fe	3.15E-05	1.30E-04	2.35E-04	2.56E-04	2.53E-04	3.29E-04	3.39E-04	3.03E-04
^{59}Fe	6.92E-06	4.66E-05	6.84E-05	5.10E-05	6.37E-05	5.98E-05	4.02E-05	8.79E-05
^{60}Fe	1.49E-05	4.82E-05	8.07E-05	2.82E-05	5.71E-05	2.40E-05	9.28E-06	9.55E-05
^{55}Co	1.84E-04	6.27E-04	3.67E-04	3.71E-04	2.73E-04	4.71E-04	3.84E-04	5.95E-04
^{56}Co	1.15E-04	2.11E-04	2.43E-04	1.66E-04	1.07E-04	2.01E-04	1.19E-04	2.07E-04
^{57}Co	3.24E-05	4.64E-05	5.17E-05	3.01E-05	2.25E-05	3.65E-05	2.52E-05	3.71E-05
^{58}Co	6.43E-06	9.31E-06	1.01E-05	5.92E-06	4.58E-06	7.77E-06	5.07E-06	7.16E-06
^{59}Co	9.24E-06	3.19E-05	5.67E-05	6.13E-05	5.94E-05	6.70E-05	6.42E-05	8.33E-05
^{60}Co	3.23E-06	5.45E-06	1.15E-05	1.35E-05	1.25E-05	1.68E-05	1.86E-05	1.14E-05
^{61}Co	6.74E-06	9.10E-06	1.70E-05	6.87E-06	8.04E-06	8.72E-06	8.08E-06	2.04E-05
^{56}Ni	6.98E-02	1.24E-01	1.48E-01	7.89E-02	8.00E-02	1.11E-01	6.78E-02	1.32E-01
^{57}Ni	4.04E-03	6.06E-03	7.24E-03	3.54E-03	3.72E-03	4.92E-03	3.21E-03	5.49E-03
^{58}Ni	9.71E-03	1.37E-02	1.38E-02	5.59E-03	5.84E-03	7.71E-03	4.87E-03	8.58E-03
^{59}Ni	2.17E-04	3.39E-04	4.37E-04	2.36E-04	1.48E-04	3.00E-04	1.90E-04	2.99E-04
^{60}Ni	9.36E-05	1.59E-04	2.42E-04	1.54E-04	1.05E-04	1.94E-04	1.42E-04	2.32E-04
^{61}Ni	5.22E-06	1.51E-05	2.60E-05	2.77E-05	2.56E-05	3.06E-05	2.89E-05	3.20E-05
^{62}Ni	1.37E-05	4.27E-05	7.35E-05	7.12E-05	7.10E-05	7.74E-05	6.63E-05	8.92E-05
^{63}Ni	4.62E-06	1.52E-05	2.15E-05	2.69E-05	2.42E-05	3.12E-05	2.95E-05	2.84E-05
^{64}Ni	1.42E-05	2.92E-05	4.16E-05	4.69E-05	4.47E-05	4.93E-05	4.22E-05	5.17E-05
^{65}Ni	7.20E-06	1.46E-05	2.39E-05	1.03E-05	1.86E-05	7.95E-06	3.18E-06	3.02E-05
^{59}Cu	7.46E-05	1.07E-04	9.58E-05	5.13E-05	1.08E-04	6.59E-05	4.04E-05	6.53E-05
^{60}Cu	1.18E-03	1.76E-03	2.54E-03	1.28E-03	8.81E-04	1.86E-03	1.12E-03	1.88E-03
^{61}Cu	1.32E-04	2.04E-04	2.64E-04	1.32E-04	9.61E-05	1.84E-04	1.19E-04	1.82E-04
^{62}Cu	6.48E-06	9.37E-06	1.03E-05	4.62E-06	2.77E-06	6.19E-06	4.07E-06	6.03E-06
^{63}Cu	1.20E-06	2.71E-06	4.68E-06	4.57E-06	4.20E-06	4.42E-06	3.72E-06	6.58E-06
^{64}Cu	3.08E-07	4.62E-07	1.02E-06	1.04E-06	1.04E-06	8.27E-07	6.61E-07	1.51E-06
^{65}Cu	2.83E-06	5.65E-06	7.87E-06	8.30E-06	7.91E-06	6.80E-06	6.02E-06	1.13E-05
^{66}Cu	1.10E-06	1.20E-06	1.37E-06	1.14E-06	1.63E-06	1.15E-06	8.51E-07	2.16E-06
^{60}Zn	8.69E-04	1.29E-03	1.62E-03	8.14E-04	1.46E-03	1.20E-03	7.06E-04	1.21E-03
^{61}Zn	4.85E-05	6.94E-05	6.88E-05	3.44E-05	8.16E-05	4.86E-05	3.09E-05	4.83E-05
^{62}Zn	1.52E-03	2.20E-03	2.23E-03	9.51E-04	1.01E-03	1.34E-03	8.71E-04	1.33E-03
^{63}Zn	8.56E-06	1.30E-05	1.35E-05	8.38E-06	6.21E-06	9.54E-06	6.38E-06	9.11E-06
^{64}Zn	5.82E-06	8.38E-06	1.25E-05	7.80E-06	4.72E-06	9.83E-06	7.08E-06	1.13E-05
^{65}Zn	2.70E-07	5.36E-07	7.09E-07	6.28E-07	5.66E-07	5.25E-07	4.02E-07	1.01E-06
^{66}Zn	2.58E-06	7.26E-06	9.06E-06	9.37E-06	9.13E-06	8.15E-06	7.56E-06	1.10E-05
^{67}Zn	3.51E-07	1.37E-06	1.67E-06	1.98E-06	1.83E-06	1.72E-06	1.80E-06	1.94E-06
^{68}Zn	3.28E-06	7.16E-06	9.41E-06	1.08E-05	1.01E-05	1.04E-05	1.11E-05	9.72E-06
^{69}Zn	2.34E-06	3.78E-06	4.16E-06	2.56E-06	3.67E-06	2.36E-06	1.22E-06	5.47E-06
^{63}Ga	3.48E-07	4.01E-07	1.57E-07	1.03E-07	6.12E-07	1.22E-07	7.05E-08	1.15E-07
^{64}Ga	6.60E-06	9.25E-06	1.28E-05	6.57E-06	7.26E-06	9.82E-06	6.26E-06	9.55E-06
^{65}Ga	6.77E-07	1.02E-06	1.08E-06	6.59E-07	6.25E-07	7.94E-07	6.32E-07	7.45E-07
^{66}Ga	5.00E-07	7.34E-07	8.70E-07	3.91E-07	2.13E-07	5.45E-07	3.90E-07	5.22E-07
^{67}Ga	1.39E-08	1.53E-08	2.05E-08	1.82E-08	1.52E-08	1.49E-08	1.60E-08	1.57E-08
^{68}Ga	3.90E-09	5.10E-09	7.23E-09	8.08E-09	7.83E-09	5.23E-09	5.17E-09	6.89E-09
^{69}Ga	3.60E-07	9.01E-07	1.07E-06	1.04E-06	9.81E-07	7.80E-07	7.36E-07	1.39E-06
^{70}Ga	3.30E-07	4.03E-07	4.29E-07	3.95E-07	4.41E-07	3.22E-07	3.09E-07	5.36E-07
^{64}Ge	1.91E-06	2.60E-06	2.91E-06	1.49E-06	4.84E-06	2.25E-06	1.41E-06	2.19E-06
^{65}Ge	2.55E-08	2.02E-08	9.96E-09	6.51E-09	6.52E-08	7.76E-09	6.98E-09	7.81E-09
^{66}Ge	3.14E-05	4.67E-05	4.69E-05	2.05E-05	2.21E-05	2.96E-05	2.05E-05	2.83E-05
^{67}Ge	6.57E-08	8.26E-08	6.76E-08	4.74E-08	5.38E-08	4.36E-08	5.81E-08	4.58E-08
^{68}Ge	2.57E-08	2.74E-08	1.70E-08	7.09E-09	7.37E-09	8.73E-09	6.92E-09	8.81E-09
^{69}Ge	6.91E-10	3.20E-09	3.80E-09	5.15E-09	4.55E-09	3.08E-09	4.00E-09	3.89E-09
^{70}Ge	3.27E-07	1.23E-06	1.50E-06	1.54E-06	1.51E-06	1.21E-06	1.44E-06	1.47E-06
^{71}Ge	1.70E-06	4.09E-06	3.88E-06	4.36E-06	4.14E-06	3.72E-06	5.09E-06	3.86E-06
Total	9.10E-01	1.43E+00	1.72E+00	1.63E+00	1.63E+00	1.96E+00	1.92E+00	1.98E+00

15 times smaller. Such a limited component is not likely to contribute in a major way to the solar abundances, though it could relate to the anomalous composition seen in some meteorites.

The peak temperature reached at the base of the helium shell in Figure 13, 1.15×10^9 K, is somewhat smaller than implied by the usual estimate $T_p = 3E_{tot}/(4\pi r^3 a)$, which for $E_{tot} = 8.5 \times 10^{50}$ ergs (Table 6) and $r = 1.5 \times 10^9$ cm would be 1.6×10^9 K. The difference is because of the extra energy in pairs when the shock hits the helium shell and the fact that only about half of the final kinetic energy at infinity is in the form of internal energy at this point.

The nucleosynthesis in all models except 7K may be criticized because of the omission of any direct calculation of hydrogen-burning nucleosynthesis and the use of a small network during helium burning. Model 7K was calculated to help quantify this uncertainty and to have at least one calculation in which nucleosynthesis was calculated in a complete, consistent fashion throughout the star's life (see § 3.1). Model 7K was a little more centrally condensed than 7A and thus, even with a piston located at a smaller mass and moved faster (Table 6), had a smaller final kinetic energy at infinity and lower mass of ^{56}Ni (following fallback in model 7A, the actual ejected nickel masses were quite similar).

Table 10 compares models 7A and 7K at two times. At carbon ignition, one compares abundances that in 7A were calculated by the Göttingen code and mapped into KEPLER (along with solar mass fractions of isotopes for which the abundance was unknown) to those determined exclusively by KEPLER using a 200 isotope network starting on the main sequence. The difference in the final abundances ejected by the supernova reflects this, but also small differences in the stars themselves (§ 3.1), especially the larger mass of the helium shell and the lesser extent of neon shell burning in model 7K. Still, the overall agreement is encouraging.

There are specific discrepancies worth discussion. ^{13}C and ^{17}O are (realistically) smaller in model 7K, though their production factors in Table 7 are small anyway. Putting a solar abundance of these isotopes into the star at carbon ignition overestimated their actual abundance. ^{18}O is larger in model 7K. This is a consequence of the different semiconvective treatment in KEPLER (Weaver & Woosley 1993) and, especially, the thicker helium shell in the model 7K presupernova. Ignoring the outer 0.22 $M_\odot$ of model 7K (i.e., the difference in helium shell mass with model 7A), the ^{18}O mass in model 7K is 5.9×10^{-4}, in good agreement with model 7A. The higher ^{23}Na abundance in model 7K is a consequence of the Ne-Na cycle that goes on during hydrogen burning (not included in model 7A). It is realistic. The other models may actually have more sodium than given in the tables.

Some of the *s*-process nuclei, e.g., ^{58}Fe, are surprisingly insensitive to being modeled incorrectly during helium burning. Apparently neutron captures during carbon and neon burning and during the explosion compensate. So long as a certain amount of ^{22}Ne is turned into magnesium *sometime*, a comparable exposure results. The higher abundance of ^{67}Zn and Ga and Ge isotopes in model 7K does show that the helium-burning *s*-process accounts for something, though. The smaller abundances of ^{30}Si, ^{31}P, and ^{46}Ca are a consequence of less neon burning in model 7K (note also the ^{20}Ne abundance itself). ^{19}F is partly produced during helium burning, though it was not included in the helium-burning network of model 7A. Its larger abundance in model 7K, though, is also a consequence of the higher neon abundance and the neutrino process.

Finally, we note that in order to be useful for chemical evolution considerations the nucleosynthesis products contained in the supernova ejecta have to be combined with those which have been ejected during the hydrostatic evolution by the W-R mass loss (Table 3). This is especially true for helium and the CNO isotopes. However, production factors for the heavier isotopes are also affected because the total (initial) mass is larger. Thus, we have compiled in Table 11 the production factors for several isotopes evaluated for the sum of supernova and wind ejecta.

Table 11 also gives the ratio ΔHe/ΔZ for our models. Hydrogen burning and convection also lead to an enhanced helium abundance in the envelopes of massive stars which, since we started with helium cores that had already lost their envelopes, was not included here. An unknown amount would be captured by binary companions (and then eventually ejected?). Thus, the numbers in Table 11 for ΔHe/ΔZ are lower limits. The comparison with a 60 $M_\odot$ sequence of WLW (which evolved a 23 $M_\odot$ helium core) suggests that they might increase by almost a factor of 2 when the contribution of the hydrogen-rich envelope is included.

4.3. *Bolometric Light Curves*

The shock breaks through the surface of these stars only a few minutes after core collapse. Because of the short sound travel time, the stellar surface and interior remain in communication right through silicon burning. Core pulsations and semidegenerate flashes may thus lead to the ejection of small amounts of matter that can influence the shock breakout, early light curve, and spectrum. Neither surface zoning nor radiation physics was adequate here to accurately characterize the ultraviolet transient generated at that time. Thermal (single-temperature) calculations in our poorly zoned models give a temperature at shock breakout of $\sim$500,000 K and a luminosity of 2×10^{44} ergs s^{-1} lasting for about 3 minutes (e.g., in model 7A). This is a shorter, fainter, hotter transient than calculated for Type IIp supernovae (Eastman et al. 1994) or (using similar physics) SN 1987A (Woosley 1988; Ensman & Burrows 1992). One expects a more accurate calculation to give a still hotter temperature and shorter duration, possibly in the vicinity of several million degrees for a few seconds (Nadyozhin & Woosley 1995).

There then follow bright transients of several days duration (Figs. 14–16) as the supernova expands and the helium recombines. These transients have been seen in many other calculations (e.g., Ensman & Woosley 1988), but never observed in an actual supernova. The principal display is radioactive, powered by the decay of ^{56}Ni and ^{56}Co and thus sensitive, for a given hydrodynamical model and nickel mass, to the treatment of the radiative opacity, gamma-ray deposition, mixing, and clumping, all to be explored below. The optical opacity here was taken to be entirely due to electron scattering with an electron density obtained by solving the full Saha equation as in WLW (see also Ensman & Woosley 1988). This is, of course, a minimum value suitable only for obtaining approximate light curves. A more physical calculation of the radiation transport in these models is in progress (Eastman, Woosley, & Langer 1995). Early results show good agreement with those presented here, though the peak is broader and $\sim$30% fainter in the detailed calculation.

Gamma-ray deposition is handled using a local scheme that deposits energy in the same zones where the radioactive decay

TABLE 10

COMPARATIVE YIELDS (in $M_\odot$): MODELS 7A AND 7K

Isotope	Model 7A C-ign.	Model 7K C-ign.	Model 7A post-expl.	Model 7K post expl.
^{4}He	4.07E-01	6.29E-01	4.01E-01	6.05E-01
^{7}Li	2.43E-13	3.15E-24	1.96E-07	3.15E-07
^{11}B	7.08E-12	4.20E-18	1.05E-06	9.91E-07
^{12}C	1.22E+00	1.15E+00	4.13E-01	4.28E-01
^{13}C	2.04E-04	9.11E-06	4.27E-05	5.74E-06
^{14}N	1.79E-07	1.21E-08	5.85E-06	5.01E-06
^{15}N	7.94E-07	1.23E-08	2.47E-05	2.44E-05
^{16}O	1.50E+00	1.40E+00	4.46E-01	3.85E-01
^{17}O	5.09E-05	7.41E-10	1.27E-05	1.95E-07
^{18}O	4.46E-04	1.43E-03	4.43E-04	1.35E-03
^{19}F	1.74E-07	3.82E-05	1.83E-05	9.17E-05
^{20}Ne	5.31E-03	5.68E-03	8.56E-02	1.65E-01
^{21}Ne	9.12E-05	2.23E-05	2.03E-04	2.07E-04
^{22}Ne	5.08E-02	5.18E-02	1.49E-02	1.98E-02
^{23}Na	1.63E-04	7.59E-04	1.40E-03	5.07E-03
^{24}Mg	9.27E-04	1.42E-03	4.72E-02	3.61E-02
^{25}Mg	3.19E-03	4.73E-03	4.60E-03	6.27E-03
^{26}Mg	7.13E-03	6.67E-03	3.77E-03	4.63E-03
^{27}Al	1.85E-04	2.17E-04	5.53E-03	4.76E-03
^{28}Si	1.35E-03	1.83E-03	7.49E-02	6.59E-02
^{29}Si	3.73E-04	3.28E-04	3.25E-03	1.26E-03
^{30}Si	6.15E-04	3.92E-04	4.83E-03	1.86E-03
^{31}P	4.68E-05	1.53E-04	1.06E-03	4.47E-04
^{32}S	1.23E-03	9.80E-04	1.92E-02	2.55E-02
^{33}S	1.37E-05	1.63E-05	1.54E-04	1.52E-04
^{34}S	6.04E-05	5.88E-05	1.69E-03	1.20E-03
^{36}S	8.40E-07	6.91E-06	9.28E-06	4.42E-06
^{35}Cl	8.68E-06	1.20E-05	1.87E-04	1.50E-04
^{37}Cl	1.36E-05	9.19E-05	2.76E-05	4.61E-05
^{36}Ar	2.36E-04	1.60E-04	2.49E-03	3.78E-03
^{38}Ar	5.45E-05	9.65E-05	4.93E-04	1.01E-03
^{40}Ar	2.58E-07	1.84E-06	2.20E-06	1.82E-06
^{39}K	1.12E-05	1.47E-05	5.75E-05	1.07E-04
^{40}K	3.21E-07	1.24E-06	3.89E-07	5.24E-07
^{41}K	2.10E-06	5.44E-06	4.06E-06	6.76E-06
^{40}Ca	1.84E-04	1.34E-04	1.71E-03	2.67E-03
^{42}Ca	1.54E-06	5.32E-06	1.26E-05	2.97E-05
^{43}Ca	3.39E-07	1.49E-06	1.14E-06	1.38E-06
^{44}Ca	4.46E-06	6.26E-06	7.03E-05	4.76E-05
^{46}Ca	1.12E-08	6.89E-09	2.02E-07	4.34E-08
^{48}Ca	4.39E-07	4.26E-07	1.84E-07	2.04E-07
^{45}Sc	1.93E-07	4.89E-07	1.17E-06	1.24E-06
^{46}Ti	7.57E-07	1.42E-06	7.99E-06	1.68E-05
^{47}Ti	5.90E-07	5.76E-07	2.01E-06	1.95E-06
^{48}Ti	6.12E-06	3.16E-06	1.36E-04	1.13E-04
^{49}Ti	1.16E-06	2.37E-06	6.13E-06	6.93E-06
^{50}Ti	8.54E-07	4.15E-06	1.37E-06	1.73E-06
^{50}V	2.19E-09	7.55E-10	5.61E-08	4.09E-08
^{51}V	1.27E-06	9.23E-07	9.11E-06	1.30E-05
^{50}Cr	1.95E-06	6.37E-07	3.67E-05	5.95E-05
^{52}Cr	4.52E-05	3.05E-05	5.16E-04	6.41E-04
^{53}Cr	5.75E-06	4.98E-06	5.94E-05	8.70E-05
^{54}Cr	5.11E-06	1.77E-05	6.28E-06	7.54E-06
^{55}Mn	5.23E-05	4.16E-05	3.33E-04	4.62E-04
^{54}Fe	1.97E-04	7.69E-05	2.53E-03	3.55E-03
^{56}Fe	3.49E-03	2.08E-03	8.12E-02	7.84E-02
^{57}Fe	2.33E-04	4.90E-04	3.91E-03	3.75E-03
^{58}Fe	1.15E-04	9.26E-04	2.58E-04	2.38E-04
^{59}Co	3.38E-05	2.59E-04	3.78E-04	3.48E-04
^{58}Ni	1.33E-04	4.80E-05	5.84E-03	6.61E-03
^{60}Ni	7.15E-05	2.54E-04	2.52E-03	2.12E-03
^{61}Ni	9.28E-06	7.49E-05	2.29E-04	2.10E-04
^{62}Ni	1.51E-05	1.24E-04	1.09E-03	1.17E-03
^{64}Ni	4.78E-06	6.87E-05	4.51E-05	7.98E-05
^{63}Cu	3.95E-06	4.08E-05	3.52E-05	6.54E-05
^{65}Cu	1.66E-06	2.11E-05	2.77E-05	2.40E-05
^{64}Zn	3.11E-06	1.41E-05	1.75E-05	1.82E-05
^{66}Zn	2.30E-06	1.89E-05	3.31E-05	4.84E-05
^{67}Zn	3.87E-07	3.59E-06	1.90E-06	5.93E-06
^{68}Zn	1.64E-06	1.26E-05	1.01E-05	2.58E-05
^{70}Zn	4.04E-15	1.87E-14	4.41E-07	6.64E-07
^{69}Ga	1.71E-07	1.38E-06	4.66E-06	4.56E-06
^{71}Ga	1.63E-07	4.05E-06	4.14E-06	1.53E-05
^{70}Ge	2.01E-07	1.73E-06	1.51E-06	4.91E-06
Total	3.20E+00	3.26E+00	1.63E+00	1.86E+00

TABLE 11

PRODUCTION FACTORS CORE + WIND

Isotope	4	5	7A	10A	20	60H[a]
^{4}He.....	3.19	2.88	2.59	2.42	2.64	...
^{12}C.....	10.8	15.7	30.5	48.9	48.9	...
^{14}N.....	10.5	9.23	7.29	5.65	3.43	...
^{16}O.....	1.83	5.08	8.19	9.98	5.38	...
^{18}O.....	33.1	44.4	62.8	44.6	55.4	...
^{20}Ne.....	1.66[b]	11.4[b]	9.50[b]	7.09[b]	5.86[b]	...
^{21}Ne.....	3.41[b]	14.5[b]	8.54[b]	4.42	6.35	...
^{22}Ne.....	11.3[b]	12.7[b]	31.9	59.3	89.0	...
^{24}Mg.....	3.07[b]	12.4[b]	16.3[b]	16.6[b]	5.22[b]	...
^{25}Mg.....	3.10[b]	12.8[b]	12.9[b]	9.86	7.29	...
^{26}Mg.....	3.61[b]	9.89[b]	9.80[b]	7.59	5.98	...
^{28}Si.....	10.6[b]	17.8[b]	22.9[b]	16.1[b]	8.32[b]	...
^{29}Si.....	4.75[b]	8.55[b]	17.0[b]	18.2	4.53	...
^{30}Si.....	8.91[b]	22.5[b]	38.5[b]	33.9[b]	10.1	...
^{32}S.....	7.28[b]	11.1[b]	10.8[b]	7.07[b]	4.95[b]	...
^{36}Ar.....	6.39[b]	11.1[b]	7.68[b]	5.42[b]	3.96[b]	...
^{56}Fe.....	23.5[b]	30.5[b]	27.9[b]	12.2[b]	7.10[b]	...
ΔHe/ΔZ...	5.6[c]	2.5[c]	1.5[c]	1.3[c]	1.8[c]	3.3

[a] Model 60WRA from WLW; here, contributions from the H-rich envelope are included.

[b] Production factor in the wind material equal to 1.

[c] Neglecting any potential H-rich envelope; its consideration could increase ΔHe by as much as a factor of 2.

occurs. The deposition fraction is calculated using the integrated column depth to the surface of the supernova and a gamma-ray opacity of 0.054 cm^2 g^{-1}. This prescription has previously given good agreement with more detailed gamma-ray transport calculations (e.g., Eastman et al. 1994).

Compared to previous work, our light curves agree well with those calculated by others for similar stellar masses and ^{56}Ni synthesized. Model 7A, for example, with properties given in Table 6, agrees well with the 3.3 $M_\odot$ helium core explosion (10^{51} ergs; 0.15 $M_\odot$ ^{56}Ni) calculated by Shigeyama et al. (1990). Compared to observations of Type Ib SN 1983N (e.g., Blair & Panagia 1987; Panagia 1987), models 5 and 7 are both in reasonable agreement (for arbitrary adjustments of explosion date and peak luminosity), though the simple light curves calculated here have peaks that are actually too *narrow* compared with the observations (especially the case for model 4). Comparison with model 10 or 20 (Figs. 14 and 15) gives better

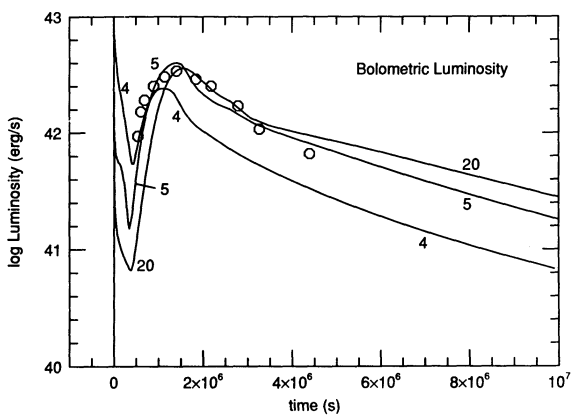

FIG. 14.—Bolometric light curves for models 4, 5, and 20 assuming an optical opacity due solely to electron scattering. Except for a brief transient at the beginning, the light curves are entirely due to radioactive decay. The open circles are data for SN 1983N from Blair & Panagia (1987) arbitrarily shifted in peak luminosity and explosion date.

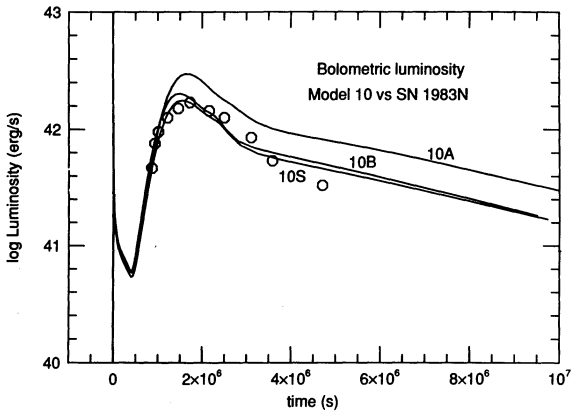

FIG. 15.—Bolometric light curves for models 10A, B, and S. The differences are almost entirely due to the different ^{56}Ni masses produced in the models (see Table 6 and Fig. 14). The open circles are data for SN 1983N from Blair & Panagia (1987) arbitrarily shifted in peak luminosity and explosion date.

agreement for SN 1983N near peak, but this may be misleading. Though our calculations employ a realistic prescription for calculating the electron scattering opacity (solution of the Saha equation for each zone and time), line opacity is not included. This will surely lead to a broader peak (see above). The fact that the single experimental point on the tail for SN 1983N lies well below the model curves is of concern. Overestimating luminosity on the tail is a long-standing problem for SN Ib models (e.g., Ensman & Woosley 1988).

Figure 16 explores one of several ways this difficulty might be addressed by reasonable alterations in the transport calculation. Our models are all one-dimensional and thus cannot directly confront the inhomogeneity likely to exist in any real supernova several weeks after its explosion. The explosion mechanism itself involves uncertain physics, but is inherently multidimensional (Herant, Benz, & Colgate 1992; Herant et al. 1994). Convection in the neutrino-energized "hot bubble" may be responsible for mixing ^{56}Ni out some distance in the star, and as the shock moves outward through regions of increasing

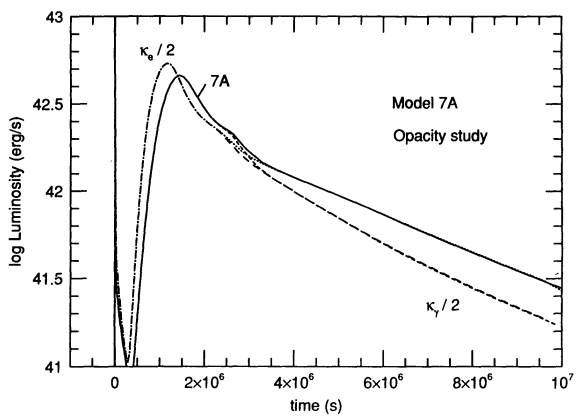

FIG. 16.—Three light curve calculations for model 7A. The solid line is the standard calculation using full Compton opacity and a gamma-ray deposition opacity of 0.054 cm^2 g^{-1}. The long-dashed line results if both the electron scattering (optical) opacity is divided by 2 (to simulate crudely the effect of clumping) and the gamma-ray opacity is reduced to 0.027 cm^2 g^{-1}. The short-dashed line (indistinguishable on the tail of the light curve) results if only the gamma-ray opacity is halved. A fourth calculation (not shown) in which only the electron scattering (optical) opacity was reduced by two is indistinguishable from the solid line after 3 × 10^6 s.

ρr^3 in the mantle, it will decelerate and Rayleigh-Taylor instabilities will occur (e.g., Herant & Woosley 1994, 1995). Clumps in the resulting mixture of ^{56}Ni and ^{16}O may be exaggerated by the decay of ^{56}Ni (Li, McCray, & Sunyaev 1993). A clumpy medium has transport properties that are different from those of a homogeneous medium having the same mass and radius. The characteristic diffusion time for optical radiation is shorter, and as the optical depth for gamma rays approaches unity (but not before), clumping can also make it easier for gamma rays to escape. Reliable multidimensional calculations are still some time away, but we illustrate the probable effect by simply decreasing the opacities used in the gamma-ray deposition calculation and radiation transport. This has been done for model 7A in Figure 16. The electron scattering opacity and gamma-ray deposition opacity have both been reduced by a factor of 2.

Reducing the ejected mass and mixing or simply increasing the uncertain expansion energy can also cause the light curve to decline more rapidly on the tail. We explore these effects in relation to a more recent Type Ic supernova, SN 1994I, for which good bolometric data has been obtained on both the tail and peak of the light curve. Schmidt, Kirshner, & Wells (1994) adopt a distance to SN 1994I of 7 Mpc and tabulate data for three different assumed reddening corrections, $A_V = 0.6$, 1.0, and 1.4. Figure 17 shows one straightforward way to get good agreement. Even though the kinetic energy of model 4 is relatively low (Table 6), the small amount of mass ejected implies a rapid decrease in the column depth after peak. Simply by scaling the mass of ^{56}Ni produced in the explosion to an appropriate value, 0.043 $M_\odot$, one obtains good agreement.

Models 4 and 5 give very different light curves (Fig. 14), but reasonable variations in model parameters can also give good agreement between SN 1994I and model 5 and, along the way, illustrate some interesting sensitivities. Holding the ^{56}Ni mass

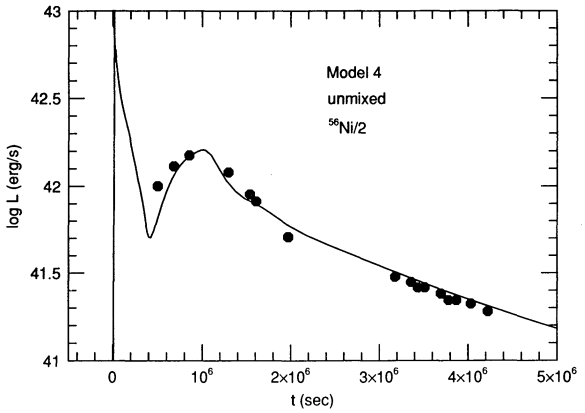

FIG. 17.—Comparison of model 4 (Table 6) to observational data for Type Ic SN 1994I (Schmidt et al. 1994). The only modification to the standard model 4 was to divide the ejected ^{56}Ni mass by about a factor of 2 (actual mass 0.043 $M_\odot$). The observational data points are based on an assumed distance of 7 Mpc, explosion date JD 9440, and reddening $A_V = 1.0$.

at an appropriate value, 0.048 $M_\odot$, Figure 18 shows that increasing the explosion energy causes the light curve to peak a little earlier, have about the same duration, and then decline faster on the tail. Mixing also changes the width of the peak very little. Moving some ^{56}Ni out leads to an earlier rise, but gamma-ray escape also causes an earlier decline. Actually, the peak is broadened a little by mixing because ^{56}Ni decay keeps the temperature hotter and the electron opacity higher in a large fraction of the mass. Shifting the center of mass of the ^{56}Ni distribution outward obviously reduces the column depth for gamma-ray absorption, and so the mixed version of the model declines more steeply on the tail, eventually, for quite extensive mixing, coming into good agreement with SN 1994I.

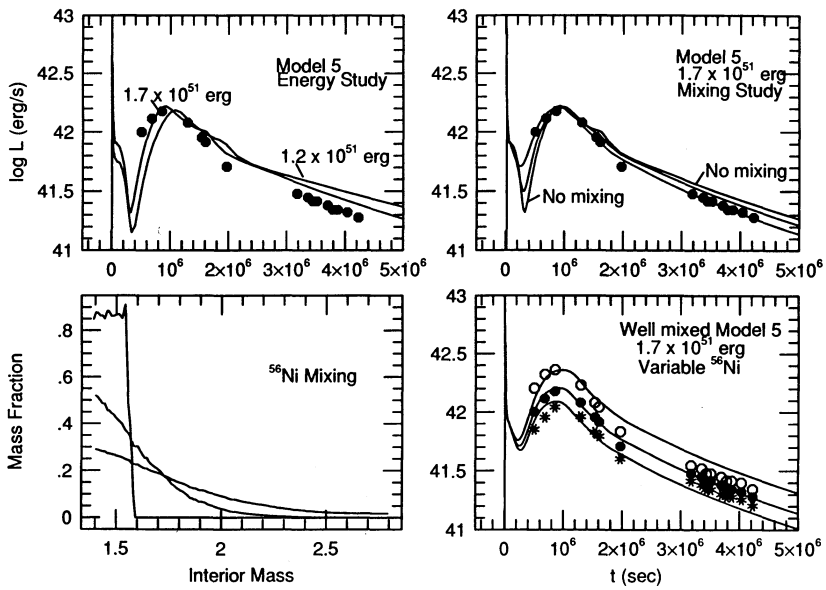

FIG. 18.—Sensitivity of the light curve for model 5 to explosion energy and mixing. The upper left panel shows the standard 5 $M_\odot$ model (Table 6) for two values of kinetic energy at infinity: 1.2 and 1.7 × 10^{51} ergs. Data points are for SN 1994I (Schmidt et al. 1994) for an assumed distance (7 Mpc), reddening ($A_V = 1.0$), and explosion date (JD 9440). The ejected ^{56}Ni mass has been adjusted to 0.048 $M_\odot$. The upper right panel shows the same 1.7 × 10^{51} erg light curve, but for three choices of ^{56}Ni mixing (*lower left panel*). The ^{56}Ni mass fraction shown in the lower left has been multiplied by 3 for ease of display. The lower right panel shows the most mixed 1.7 × 10^{51} erg explosion (i.e., lowest curve on the tail in the upper right) for three choices of ^{56}Ni mass (0.035, 0.048, and 0.071 $M_\odot$) and three choices of reddening for the data ($A_V = 0.6$, 1.0, and 1.4).

Uncertainty in the reddening changes not only the peak luminosity, but also the ratio of peak to tail luminosities. Figure 18 also shows that variation of the total ^{56}Ni mass (0.035, 0.048, and 0.071 $M_\odot$ for a distance of 7 Mpc) can fit the range of observational uncertainty. See also § 5 and Nomoto et al. (1994) for further discussion of SN 1994I.

Finally, we mention the interesting and challenging case of subluminous Type Ia supernovae. The prototype for these is considered to be SN 1991bg. This supernova has been classified Type Ia owing to the defining 6150 Å silicon absorption feature near maximum. It also occurred on the outskirts of an elliptical galaxy, NGC 4374, and thus is probably not the outcome of massive stellar evolution. It has been modeled, with reasonable success, as the explosion of a sub–Chandrasekhar-mass white dwarf (Ruiz-Lapuente et al. 1993; Woosley & Weaver 1994), but the low mass of ^{56}Ni required to explain the subluminous light curve ($\sim$0.15 $M_\odot$; Phillips 1993) may be difficult to achieve, and the robust nature of the central detonation has yet to be demonstrated for such low-mass white dwarfs when calculated in more than one dimension. Were it not for the association with an elliptical galaxy, it would be tempting to associate SN 1991bg with some of the models presented here. An appropriate light curve could easily be constructed, and whether massive star models always lack the silicon absorption feature at 6150 Å has yet to be demonstrated (in fact, it has yet to be demonstrated that it is absent in *any* massive star model). However, we will not speculate further about SN 1991bg and merely point out that there are other similar supernovae (e.g., SN 1992K; Hamuy et al. 1994) that *do* occur in spiral galaxies. It is possible that both massive stars and exploding dwarfs contribute to this sample.

5. STELLAR WIND MASS LOSS OR BINARY MASS EXCHANGE?

So far our calculations have centered on helium stars experiencing mass-dependent mass loss. For most of the stars considered, especially $M_\alpha \lesssim 10\ M_\odot$, radiation-driven winds alone would not have removed the hydrogen envelope; thus, our models are presumably in mass-exchanging binary systems (cf. § 1). Except for its role in removing the hydrogen at an early stage, however, we have considered the companion to be inert in the later stages of evolution. Given the small radii of our cores (Table 2), this seems a reasonable assumption in most cases.

However, it is possible that the helium star experiences additional mass transfer very late in its evolution provided that the hydrogen envelope was lost through the formation of a common envelope (e.g., Bhattacharya & van den Heuvel 1991; Nomoto et al. 1994). The secondary can then be close enough to provoke a second stage of mass transfer (case BB; Delgado & Thomas 1981) after helium has been depleted in the core of the primary. This occurs during the brief time in which the star makes the readjustment to a helium shell burning luminosity source and during carbon burning itself.

To illustrate how the final presupernova star might differ in this situation, we have evolved several models including the effects of simulated mass transfer to a very nearby companion at late times. The uncertainties in this sort of calculation are to be emphasized. Besides the poorly understood nature of common envelope evolution itself, the transfer rates, conservative nature of the transfer, and fate of the secondary star are poorly determined, if at all. Still, it is interesting to explore such cases to put limits on the necessary conditions and determine possible outcomes, if only qualitatively. In what follows we consider conservative mass transfer, though the code has provision for nonconservative transfer (Podsiadlowski et al. 1992; Woosley et al. 1994).

Our first such study was based on model 5A. We take as our starting point the Göttingen model shortly after the time of link (helium was depleted and the central temperature was 6×10^8 K). Once relaxed into the KEPLER code, the radius of this star was 9.3×10^{10} cm, and the luminosity 1.8×10^{38} ergs s^{-1}. A 2 $M_\odot$ companion (perfectly absorbing point mass) was then introduced at 0.02 AU. This is a lower limit for the radius a main-sequence companion star might occupy without immediately merging into the primary. Typical radii of 2 $M_\odot$ main-sequence stars are 3 $R_\odot = 0.014$ AU. Mass transfer began about 4000 yr later when the central temperature was 7.4×10^8 K, carbon burning was already in progress [$X_c(^{12}\mathrm{C}) = 0.28$, down from 0.38, initially], and the radius had reached the Roche radius, 1.22×10^{11} cm. The mass of the primary at this point was 2.82 $M_\odot$. Mass transfer then occurred at a self-limiting rate for the next 8000 yr. The implementation of mass transfer in the code was the same as in Woosley et al. (1994).

Although the code allowed, in principle, a maximum transfer rate of $5 \times 10^{-4}\ M_\odot$ yr^{-1} (parameter setting), the star found a natural rate closer to $5 \times 10^{-5}\ M_\odot$ yr^{-1}. The mass of the primary dropped to 2.62 $M_\odot$ in the first 4000 yr. This maximum exchange rate reflects the fact that mass loss from the primary is limited by the efficiency with which luminosity can lift material out of its potential well to the Roche radius (Woosley et al. 1994). One half-solar-mass interior from the surface, the radius is typically 10^{10} cm, and the gravitational potential 3×10^{16} ergs g^{-1}. The luminosity can only raise $\sim 10^{-4}\ M_\odot$ yr^{-1} to the Roche radius. In fact, not all the luminosity is available for this purpose, but then the internal energy is comparable to the gravitational energy. That the star chose to transfer an average of $\sim 10^{-4}\ M_\odot$ yr^{-1}, despite a numerical cap that would have allowed more, seems reasonable.

By the end of its evolution the mass of the primary had declined from 2.82 to 2.38 $M_\odot$ (2.43 $M_\odot$ at the end of carbon burning). The primary was still almost filling its Roche lobe ($R_{\mathrm{Roche}} = 1.06 \times 10^{11}$ cm), but mass transfer effectively ceased when the masses of the primary and secondary became equal. Any further (conservative) transfer would have driven the secondary farther away. The composition of the final star is given in Figure 19, which may be compared to Figure 8 evolved without late binary transfer. Had either the mass of the primary or the initial separation been larger, the transfer would have been less and Figure 8 more representative. Had the mass of the secondary been less, more mass could have been transferred. It seems unlikely to us, however, that a primary derived from a 17 $M_\odot$ main-sequence star (model 5) would have a main-sequence star of such low mass as a close companion during carbon burning. If nothing else, one must be concerned about where all the mass from the (originally 20 $M_\odot$) primary went (presumed all lost from the system).

We thus considered two other models that had a presumed neon-oxygen white dwarf as a nearby companion. How this might be achieved has been discussed by Nomoto et al. (1994). Because we are interested, in this section, in exploring stars that might have a minimal helium layer when they explode, we considered models with a somewhat larger carbon-oxygen core than model 5, namely, model 7K (the KEPLER-derived equivalent of model 7A). Model 7K at helium depletion (3.23 $M_\odot$)

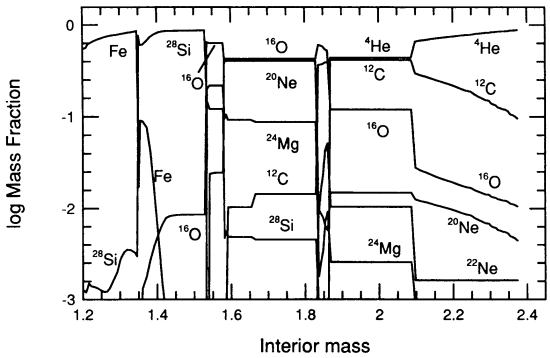

FIG. 19.—Model 5A was recalculated during its post–helium-burning phase by assuming, not mass-dependent mass loss, but conservative mass transfer to a very close binary companion (initially 2 $M_\odot$ at 0.02 AU); see text. The final composition of the presupernova star shown here reveals a thinner, but still substantial shell of unburned helium (compare to Fig. 8); see text. The final helium mass in the outer layers of the star is 0.33 $M_\odot$. The surface mass fraction is 0.88.

was first given a companion of 1.2 $M_\odot$ at a radius of 0.015 AU. The radius of model 7K at that time was 2.5×10^{10} cm, and the Roche radius 1.0×10^{11} cm. The luminosity was 8.5×10^{37} ergs s^{-1}. No transfer was occurring. By the time the central temperature reached 6×10^8 K, the primary radius was still only 6.8×10^{10} cm and no transfer was occurring. Fifty thousand years after the beginning of the calculation, when the star was already halfway through carbon burning (X_c down from 0.37 to 0.20), the primary filled its Roche lobe and transfer commenced. At this point, the primary's luminosity was 2.7×10^{38} ergs s^{-1}, and the central temperature $T_c = 7.8 \times 10^8$. Over the next 3000 yr the mass of the primary decreased from 3.23 to 2.73 $M_\odot$. This time the final mass was not equal to one-half of the sum of the initial primary and secondary masses and the secondary was still accreting and moving closer when the primary died. Despite the substantial mass transfer, the final star still had a substantial helium layer in place (Fig. 20*a*).

For our final calculation, the most extreme, model 7K was recalculated with the same white dwarf moved in to 0.0075 AU, not much more than the radius of the primary at helium depletion. The radius of the initial primary was (again) 2.5×10^{10} cm (at $T_c = 2.7 \times 10^8$ K), but the Roche radius was half as much as before, 5.2×10^{10} cm. Mass transfer commenced 40,000 yr after this starting point, in this case shortly before carbon ignition ($T_c = 5 \times 10^8$ K; luminosity = 2.2×10^{38} ergs s^{-1}). During the next 12,000 yr the primary lost 0.83 $M_\odot$ to end its life as a 2.40 $M_\odot$ star. The mass lost included almost, but not quite all of the helium shell (Fig. 20*b*). Again, the final mass was not half of the sum of the initial masses, and the carbon core was not completely uncovered. Mass exchange had already stopped before the primary died. There were two reasons why more mass was not transferred. First, there was inadequate time to remove additional mass. The mass transfer rate is limited by the Kelvin-Helmholtz timescale of the envelope (see above). Second, removing the helium layer eventually puts out the helium-burning shell which is providing most of the luminosity of the presupernova star. At that point the primary can shrink rapidly and truncate the transfer (see also Biermann & Kippenhahn 1971).

While the composition of these stars differed from those considered elsewhere in this paper, and that will have spectroscopic consequences, the structure was virtually identical to

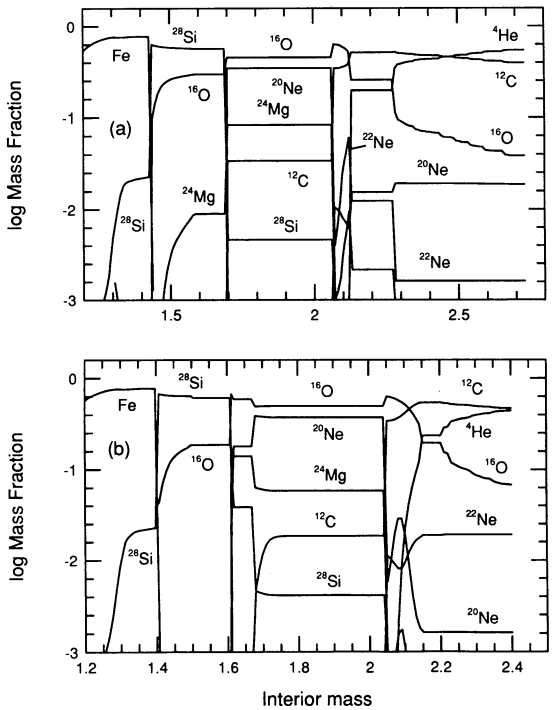

FIG. 20.—Model 7K was recalculated during its post–helium-burning evolution assuming a neon-oxygen white dwarf of mass 1.2 $M_\odot$ located (*a*) 0.015 AU and (*b*) 0.0075 AU. The final presupernova composition is shown. Compare to Fig. 9. In (*a*) the total helium mass in the presupernova star (outside of the iron core) is 0.25 $M_\odot$ and the surface mass fraction is 0.54. The corresponding quantities for (*b*) are 0.09 $M_\odot$ and 0.43.

other models having the same final mass. Since the three cases considered here all end up with 2.4–1.7 $M_\odot$, they resemble closely models 4 and 5. Further, since the light curves depend only on the masses and presupernova density structure, the bolometric display of these stars, when they explode, should be virtually identical to those of models 4 and 5 (Figs. 14, 17, and 18). In particular, any one of these models would be a good match to SN 1994I and presumably other Type Ic supernovae (see also Nomoto et al. 1994).

6. CONCLUSIONS

Using a reasonable (though admittedly uncertain) prescription for mass loss, we find that massive stars ($M \gtrsim 15\ M_\odot$ on the main sequence) whose helium cores are uncovered prior to or early in helium burning will converge on a common final mass in the range 2.3–5.5 $M_\odot$ (Tables 2 and 6). These cores have been evolved through advanced nuclear burning stages to the endpoint of their stable evolution and then exploded using a piston prescription and energy that realistically reflect core collapse and a neutrino-powered supernova in a massive star (Table 6). The resultant light curves are similar to what is observed in Type Ib and Ic supernova (Figs. 14–18; §§ 4.3 and 5).

Though we have modeled mass loss numerically using a prescription that might be appropriate for single stars, our final results are similar to what one might obtain in a mass-exchanging binary. Our model 4, for example, is very similar in composition and structure to a 2.5 $M_\odot$ helium core evolved in a close binary by Habets (1986, Fig. 11). The final mass of his model was 2.2 $M_\odot$, similar to model 4, and though he halted his evolution at neon ignition, the structure of the outer layers

should not change much during later stages. Binary evolution has also been considered explicitly in § 5.

While the spectroscopic diagnostics of our models have yet to be computed, the results are likely to differ from what is obtained from a calculation that does not follow the nuclear burning and mass loss together. The receding helium convective layer leaves behind abundance profiles that are different from what exists at the outer boundary of a helium core evolved at constant mass (Figs. 7–11; see also WLW). Despite the convergence to a common supernova progenitor mass, the composition retains some memory of the original mass of the progenitor. Thus, the lowest mass models have a surface that is nearly 100% helium with a trace of nitrogen, while for the highest mass models (e.g., Fig. 11), helium is less abundant than carbon and oxygen is also quite abundant. Spectra taken at early times might reflect these differences, and even late-time spectra may show high-velocity wings reflecting the surface composition.

However, even including the special cases treated in § 5, none of the models studied here is so extreme as to remove all the helium from its surface. Even model 20 has 34% helium at the surface and 12% when averaged over all the ejecta (0.22 $M_\odot$ of ^{4}He), and the most extreme case considered in § 5 (Fig. 20*b*) still had 0.09 $M_\odot$ of ^{4}He with a surface mass fraction of 0.43. This may or may not be in conflict with the conclusions of Swartz et al. (1993) who specify that SN 1987M, a nominal Type Ic supernova, must have exploded with a very low surface helium abundance. Since a 20 $M_\odot$ helium core characterizes a main-sequence star of 45–50 $M_\odot$, one interpretation of their results would be that the SN Ic comes from an extremely massive population. Model 60WRA of WLW ended its life with a helium surface abundance of 23% and an overall helium fraction in the ejecta of 7%, but such explosions would be rare. Careful tailoring of the mass-loss history might produce thinner helium layers than calculated here by, e.g., removing a proportionately larger fraction of the mass at a later time. As it is, the helium convective core recedes in response to the mass loss, leaving a thick shell with a gradient of unburned helium.

After our paper was submitted, Nomoto et al. (1994) speculated that SN 1994I, a Type Ic supernova, and by implication other Type Ic supernovae, might be the product of explosions in massive stars which, by virtue of evolution through a common envelope stage with a close binary companion, lost essentially all their helium to become bare carbon-oxygen cores. The referee asked us to comment on this, and we prepared § 5 in response.

It is our conclusion that the production of bare CO cores is difficult for the reasons given in § 5, the principal ones being a physical limit on the rate at which mass transfer can occur during carbon burning and the fact that the primary will shrink rapidly once the helium-burning shell is uncovered. We have shown, however, that it is possible, in some circumstances (Fig. 20*b*), to remove almost all of the helium layer, thus essentially confirming the Nomoto et al. hypothesis. Whether this happens in a sufficient number of stars or is required in order to explain Type Ic supernovae remains to be demonstrated. Since the light curves only distinguish the mass of ^{56}Ni and the specific energy (KE/M) of the ejecta, our earlier models for SN 1994I (models 4 and 5; Figs. 17 and 18) without late case BB mass transfer are as good. In fact, the explosion of the models discussed in § 5 would produce identical light curves. More work is needed on the spectral synthesis calculations in order to distinguish the models. A spectral diagnostic calculation would have to be able to resolve clearly the difference between 0.1 $M_\odot$ of helium and 0.3 $M_\odot$ of helium. Masses of helium significantly below 0.1 $M_\odot$ do not seem very likely.

Nucleosynthesis has been studied in detail (Tables 7–10), including one run (model 7K) which was calculated using a 200 isotope network in every zone all the way from the main sequence. Many other models were studied using the large network after carbon ignition and a network reasonably accurate up to mass 28 during helium burning. These studies show a mass of ^{56}Ni produced during the explosion in the range 0.07–0.15 $M_\odot$, narrow considering the range of model masses and parameters. This is smaller by a factor of 4 or more than the ^{56}Ni made in a Type Ia supernova based on carbon deflagration (Thielemann, Nomoto, & Yokoi 1986) and several times smaller than produced in the detonation of sub–Chandrasekhar-mass dwarfs (Woosley & Weaver 1994). Type I supernovae derived from these models are therefore fainter at maximum than Type Ia, our simple one-temperature calculations suggesting $L_{\max} = (1.5\text{–}4) \times 10^{42}$ ergs s^{-1}. More realistic models with opacity due to sources other than electron scattering would have broader, fainter light curves.

In terms of overall nucleosynthesis, though no one would claim that Type Ib supernovae are responsible for synthesizing the bulk of heavy elements in our Galaxy, the ratios to solar abundances are not bad (Table 7) for several dozen isotopes in the mass range 7–64. It is also possible that a limited r-process occurs in the helium shells of some of our models (Fig. 13). The models also produce interesting quantities of ^{26}Al and ^{60}Fe (Table 9), long-lived candidates for gamma-ray astronomy.

Our models also produce significant quantities of helium. Including the helium lost in the hydrogen envelope, the wind from the helium core, and the helium ejected in the explosion itself, ΔHe/ΔZ exceeds 2 and may approach 4 (Table 11). This is much greater than the overall average for massive stars that become supernovae without appreciable mass loss. Timmes, Woosley, & Weaver (1995) estimate the latter to be $\sim$1.3. Speculation that observed values of ΔHe/ΔZ may require that stars above a critical mass collapse to black holes (e.g., Maeder 1992, 1993; Brown & Bethe 1994, 1995), should be tempered by these results. In fact, it may be the largest stars that, for near solar metallicity, produce the greatest ΔHe/ΔZ when mass loss is properly included.

One of the defining characteristics of Type Ib supernovae is the 6150 Å lines of Si II in the peak light spectrum. Type Ia has the feature; Type Ib does not. The simplest solution to this observation would be for the Type Ib supernova to be noticeably deficient in silicon. All our models make silicon and iron in roughly solar proportions (Tables 7 and 8) and eject 0.02–0.09 $M_\odot$ of ^{28}Si (Table 4). The most common variety Type Ib would probably come from the lower mass progenitors so perhaps 0.04 $M_\odot$ of silicon might be typical. This is less, but not much less than Type Ia. Thielemann et al. (1986) find 0.15 $M_\odot$ of silicon made in model W7, but many other calculations of carbon deflagration give less. Sub–Chandrasekhar-mass models for Type Ia supernovae (Woosley & Weaver 1994) give 0.04–0.14 $M_\odot$. Perhaps the ionization state of the silicon is different here owing to the different nature of the explosions and resulting ^{56}Ni and density profiles. Our models do produce a lot of oxygen, and that should be beneficial in modeling the late-time spectra of Type Ib. However, until the peak light spectra of these models has been reliably calculated, it cannot be concluded that they are exclusively Type Ib progenitors. *Some of them could be Type Ia.* As such they would occur

in star-forming regions, have fainter than typical Type Ia light curves, and leave neutron star remnants.

The baryonic masses of the bound remnants also span a limited range, 1.35–1.59 $M_\odot$ (Table 6). This is, in large measure, set by choosing the location of the piston in the explosion model, but there is some feedback (§ 4). Models in which the piston is situated too deeply experience significant fallback if the final kinetic energy is not to be much greater than 10^{51} ergs (models 7A, 10A, and 20). Also nucleosynthesis would not allow the siting of the piston much inside of the neutronized iron core and the light curve requires that ^{56}Ni be ejected. Typical baryonic remnants are about 1.55 $M_\odot$, which after all neutrino losses would imply a neutron star gravitational mass near 1.4 $M_\odot$. This is consistent with the observed average neutron star mass, 1.35 ± 0.27 $M_\odot$ (Thorsett et al. 1993).

The models presented here are similar in many ways to model 60WRA of WLW, the 4.25 $M_\odot$ remnant of a main-sequence 60 $M_\odot$ star. Model 20 here is especially similar. How might the endpoints of very massive single stars and less massive binary stars be distinguished? Once the stars have converged to such a common final mass there will be little that could be observed in the supernova to distinguish their prior evolution. However, for single stars to produce Type Ib supernovae, which probably requires a final core substantially smaller than a $M \gtrsim 30$ $M_\odot$ main-sequence star could produce by simply losing its envelope, one expects a large fraction of the helium core to have been lost. Thus, the surface abundances would more likely be rich in carbon and oxygen (WC and WO progenitors) and less so in helium (WN progenitor). This difference would be reflected in the highest velocity material visible in the spectrum. Since the single stars may lose their envelopes, on the average, later than stars in binaries, they may end up with larger helium cores and produce light curves that are broader and fainter and spectra that are helium deficient.

Are there enough of the stars we have studied in this paper to explain the observations of Type Ib supernovae? Podsiadlowski et al. (1992) have systematically explored the presupernova evolution of massive stars in interacting binaries. Based on Monte Carlo simulations and a Salpeter initial mass function they conclude that 13% (one binary for every three systems) to 26% (two binaries for every three systems) of massive stars may end their lives as Type Ib supernovae (most of the remainder are Type IIp). This would be enough to explain the observational sample. Thus it may be that single stars contribute negligibly to the Type Ib sample or perhaps form a separate category altogether (SN 1985F?).

The calculations of Podsiadlowski et al. (1992, 1993) also suggest a familar relation between Type Ib supernovae and "stripped supernovae" (their term) such as SN 1993J, an event we have elsewhere referred to as a "Type IIb" supernova (Woosley et al. 1994). Events like SN 1993J would arise from binaries that experience case C mass transfer late in their evolution.

This work has been supported by the National Science Foundation (NSF 91 15367); the NASA Theory Program (NAGW 2525); the Deutsche Forschungsgemeinschaft (La 587/8-1); and, at Livermore, by the Department of Energy (W-7405-ENG-48). We thank Craig Wheeler and Ron Eastman for educational discussions regarding Type Ic supernovae and supernova spectroscopy in general.

REFERENCES

Anders, E., & Grevesse, N. 1989, Geochim. Cosmochim. Acta, 53, 197
Azuma, R. E., et al. 1994, Phys. Rev. C, 50, 1194
Bhattacharya, D., & van den Heuvel, E. P. J. 1991, Phys. Rep., 203, 1
Biermann, L., & Kippenhahn, R. 1971, A&A, 14, 32
Blair, W. P., & Panagia, N. 1987, in Exploring the Universe with the *IUE* Satellite, ed. Y. Kondo et al. (Dordrecht: Reidel), 549
Brown, G. E., & Bethe, H. A. 1994, ApJ, 423, 659
———. 1995, ApJ, submitted
Caughlan, G. A., & Fowler, W. A. 1988, Atomic Data and Nuclear Data Tables, 40, 238
Clayton, D. D. 1968, Principles of Stellar and Nucleosynthesis (Chicago: Univ. Chicago Press)
De Greve, J.-P., & de Loore, C. 1992, A&AS, 96, 653
Delgado, A. J., & Thomas, H.-C., 1981, A&A, 96, 142
de Loore, C., & De Greve, J.-P. 1992, A&AS, 94, 453
Eastman, R., Woosley, S. E., & Langer, N. 1995, in preparation
Eastman, R., Woosley, S. E., Weaver, T. A., & Pinto, P. A. 1994, ApJ, 430, 300
Ensman, L. M., & Burrows, A. 1992, ApJ, 393, 742
Ensman, L. M., & Woosley, S. E. 1988, ApJ, 333, 754
Glatzel, W., Kiriakidis, M., & Fricke, K. J. 1993, MNRAS, 262, L7
Habets, G. M. H. J. 1986, A&A, 165, 95
Hamann, W.-R., Koesterke, L., & Wessolowski, U. 1993, A&A, 274, 397
Hamuy, M., et al. 1994, AJ, 108, 2226
Hashimoto, M., Nomoto, K., Tsujimoto, T., & Thielemann, F.-K. 1993, in Nuclei in the Cosmos, ed. F. Käppeler & K. Wisshak (Bristol: Inst. Phys. Pub.), 587
Herant, M., Benz, W., & Colgate, S. A. 1992, ApJ, 395, 642
Herant, M., Benz, W., Hix, W. R., Fryer, C. L., & Colgate, S. A. 1994, ApJ, 435, 339
Herant, M., & Woosley, S. E. 1994, ApJ, 425, 814
———. 1995, in preparation
Hsu, J. J. L., Joss, P. C., Ross, R. R., & Podsiadlowski, P. 1995, ApJ, submitted
Lamers, H. J. G. L. M., Maeder, A., Schmutz, W., & Cassinelli, J. P. 1991, ApJ, 368, 538
Langer, N. 1989a, A&A, 210, 93
———. 1989b, A&A, 220, 135
———. 1991, A&A, 252, 669
Langer, N., Hamann, W.-R., Lennon, M., Najarro, F., Pauldrach, A. W. A., & Puls, J. 1994, A&A, 290, 819
Li, H., McCray, R., & Sunyaev, R. A. 1993, ApJ, 419, 824
Maeder, A. 1983, A&A, 120, 113
———. 1991, A&A, 242, 93
———. 1992, A&A, 264, 105
———. 1993, A&A, 268, 833
Nadyozhin, D., & Woosley, S. E. 1995, in preparation
Nomoto, K., & Hashimoto, M. 1988, Phys. Rep., 163, 13
Nomoto, K., Yamaoka, H., Pols, O. R., van den Heuvel, E. P. J., Iwamoto, K., Kumagai, S., & Shigeyama, T. 1994, Nature, 371, 227
Panagia, N. 1987, in High Energy Phenomena around Collapsed Stars, ed. F. Pacini (Boston: Reidel), 33
Phillips, M. M. 1993, ApJ, 413, L105
Podsiadlowski, P., Hsu, J. J. L., Joss, P. C., & Ross, R. R. 1993, Nature, 364, 509
Podsiadlowski, P., Joss, P. C., & Hsu, J. J. L. 1992, ApJ, 391, 246
Ruiz-Lapuente, P., et al. 1993, Nature, 365, 728
Schaerer, D., & Maeder, A. 1992, A&A, 263, 129
Schaerer, D., Meynet, G., Maeder, A., & Schaller, G. 1993, A&AS, 98, 523
Schaller, G., Schaerer, D., Meynet, G., & Maeder, A. 1992, A&AS, 96, 269
Schmidt, B., Kirshner, R. P., & Wells, L. 1994, private communication
Shigeyama, T., Nomoto, K., Tsujimoto, T., & Hashimoto, M. 1990, ApJ, 361, L23
Smith, L. F., & Maeder, A. 1991, A&A, 241, 77
Swartz, D. A., Filippenko, A. V., Nomoto, K., & Wheeler, J. C. 1993, ApJ, 411, 313
Thielemann, F.-K., Nomoto, K., & Yokoi, K. 1986, A&A, 158, 17
Thielemann, F.-K., Nomoto, K., & Hashimoto, M. 1993, Les Houches Summer School 54, ed. S. Bludman, R. Mochkovitch, & J. Zinn-Justin (Amsterdam: Elsevier)
Thorsett, S. E., Arzoumanian, Z., McKinnon, M. M., & Taylor, J. H. 1993, ApJ, 405, L29
Timmes, F. X., Woosley, S. E., & Weaver, T. A. 1995, ApJS, 98, 617
Tutukov, A. V., Yungelson, L. R., & Iben, I. 1992, ApJ, 386, 197
Uomoto, A. 1986, ApJ, 310, L35
Vanbeveren, D. 1991, A&A, 252, 159
Vanbeveren, D., & de Loore, C. 1993, in ASP Conf. Ser., 104, Massive Stars: Their Lifes in the Interstellar Medium, ed. J. P. Cassinelli et al. (San Francisco: ASP), 257
van der Hucht, K. A. 1992, A&A, Rev., 4, 123
Vrancken, M., De Greve, J.-P., Yngelson, L., & Tutukov, A. 1991, A&A, 249, 411

Weaver, T. A., & Woosley, S. E. 1993, Phys. Rep., 227, 65
———. 1995, in preparation
Weaver, T. A., Zimmermann, Z. B., & Woosley, S. E. 1978, ApJ, 225, 1021
Wheeler, J. C. 1990, in Supernovae, ed. J. C. Wheeler et al. (Singapore: World Scientific), 1
Wheeler, J. C., & Levreault, R. 1985, ApJ, 294, L17
Woosley, S. E. 1988, ApJ, 330, 218
Woosley, S. E., Eastman, R., Weaver, T. A., & Pinto, P. A. 1994, ApJ, 429, 300
Woosley, S. E., Hartmann, D., Hoffman, R., & Haxton, W. 1990, ApJ, 356, 272
Woosley, S. E., Langer, N., & Weaver, T. A. 1993, ApJ, 411, 823 (WLW)
Woosley, S. E., & Weaver, T. A. 1988, Phys. Rep., 163, 79
———. 1994, ApJ, 423, 371
———. 1995, ApJS, in press